TO THE PLANNING INSPECTORATE

EN010158 Rosefield Energy farm

Application by Rosefield Energy Farm Limited for the Rosefield Solar Farm for an Order Granting Development consent for the Rosefield Energy Farm pursuant to The Planning Act 2008.

To the Examining Authority (ExA)

FIRST WRITTEN REPRESENTATION OF

PROFESSOR PETER JAMES DOBSON OBE, BSc, PhD, MA,

EMERITUS PROFESSOR OF OXFORD UNIVERSITY

[Lodged on behalf of Claydons Solar Action Group - CSAG]

1. I am Professor Peter James Dobson, OBE, BSc, PhD S'ton, MA Ox, Emeritus Professor of Oxford University. I have spent my whole adult life in the study and research into Physics and Engineering. I was appointed Professor in the Department of Engineering Science in the University of Oxford in 1996 and retired from that post in 2013. I have continued my interest in Engineering Sciences since then and continue to work in the field.

2. In 2024 my interest, experience and researches led me to prepare, jointly with a colleague, a paper/article entitled ***'Remarks on the Safety of Lithium-Ion Batteries for Large-Scale Battery Energy Storage Systems (BESS) in the UK'*** which was first published online on 21 December 2024 in the journal **Fire Technology** (Springer). (DOI: 10.1007/s10694-024-01682-x). This article was followed in February 2025 by a ***'Briefing Note: LITHIUM-ION BATTERY ENERGY STORAGE SYSTEMS (LiBS)'*** prepared by me with support from Professor (Emeritus) Peter Edwards, Professor (Emeritus) Allison Wade and Professor Sir David Melville CBE.

3. I draw attention to the first article because it was then, and still remains, the substance of my opinion on the present level of risk to the public "from fire, explosion and toxicity and the attendant clear dangers to employees at these facilities, to First-Responders, Firefighters and the local population as well as to their impact on the environment"; and this remains in my view fundamentally true to this day.

4. In the article I pointed out that "All the current generation of lithium-ion batteries always carry an inherent risk of so-called 'thermal runaway' which can result in fires, explosions and off/out gassing and toxic gases." So far as I am aware, that too remains the position with Lithium-Ion batteries today. The thermal runaway and its consequences may occur from overcharging of a battery or a defect arising during the manufacture, transport or handling of the battery.

5. "Such fires and explosions cannot be handled like a 'normal' fire – they cannot be extinguished by smothering, for example, as they do not require oxygen to sustain them. As such these incidents

often last for extended periods of time (days or weeks) and re-ignition is not uncommon." [see 'Briefing Note'].

6. And it was true then and remains true now that "Currently in the UK, …., there are no established standards and regulations concerning the safety standards of these large BESS installations …". There is 'guidance' but no statutory obligations on the Applicant. DEFRA amongst others is currently calling for a consultation on this issue. The dangers are very clear and any granting of permission without such Standards and Regulations in place is irresponsible and will make the applicants and the bodies that grant approval open to litigation. Do the developers have Insurance for the eventuality of a BESS failure?

7. The Applicant has carried out a fairly comprehensive Atmospheric Dispersion Modelling Study (ADMS) **EN010158 App 7.13** and this has produced data for most of the likely gases emitted and the larger particulate matter in the smoke. However, no details were given of the actual type of BESS system for which this was done, although the report does say that this will be repeated at the final design stage. This is re-assuring, but there are suggestions that organophosphorus compounds can be emitted from lithium ferro phosphate battery fires (Bergström, U., et al., *Vented gases and aerosol of automotive Li-ion LFP and NMC batteries in humidified nitrogen under thermal load*, in *Försvarets Forskningsinstitut FOI*. 2015.)

8. The other reason why the MWh of the battery cells needs to be known is that the level of energy stored in the battery cells will determine whether Hazardous Substances Consent [HSC] will be required: Hazardous Substance Consents for batteries of the scale implied in this application are most likely required for the transportation of LiBESS units and for large scale LiBESS installations. It is clear that Li-ion BESS of capacity >50 MWh, regardless of cell type, should carry an obligation to secure a Hazardous Substances Certificate [HSC] obligation: see the paper by Eur Ing Dr Edmund Fordham and Professor Sir David Melville entitled '***Hazardous Substances potentially generated in "loss of control" accidents in Li-ion Battery Energy Storage Systems (BESS)'***. Each 4MWh battery container unit contains several tonnes of flammable liquid electrolyte in addition to the electrical energy. Unless HSC has been applied for and granted, it would appear that an offence under s. 23 of the Planning (Hazardous Substances) Act 1990 has occurred. In this case, given the likely size and energy capacity of the LiBESS, the Applicant needs to apply for Hazardous Substances Consent (HSC) before transporting the Batteries to site and/or putting them into a BESS installation. The developer should consult with the relevant authorities on this during the consenting stage, NOT post consent. There has to my knowledge, thus far, been no such consultation.

9. However, there is a big concern about the proximity of the site to a farm where animals are raised for contribution to serum for medical applications. Noxious fumes could contaminate the surrounding farmlands and seriously impact the business of TCS Biosciences who play an important role in the UK medical infrastructure. This is a very environmentally sensitive area and in the event of a fire, the firewater must be contained properly and disposed of safely after removal of contaminants. "Fluorinated compounds in the fumes and the firewater are toxic – even in small amounts – and have a long lifetime in the environment, which could last for decades." [See ***Briefing***

Note 2025 ibid.] The Applicant does not seem to appreciate the gravity of such issues and the planning authority and the Government need to be aware of this.

10. The conclusion to which I came in 2024 and again in my Briefing Note in 2025 was that "there must now be a clear pause in allowing any BESS construction in the UK until the necessary, complete Health and Safety dangers, protocols and procedures have been established by law. These requirements are indisputable if catastrophic, safety to life event in BESS facilities are to be minimised or ideally eliminated".

11. The point is that if there is not a clear pause, applicants will continue to allow themselves the luxury of choosing whatever batteries they wish to provide for any BESS and MWh capacity of their choosing. Although I accept that there is always the chance that technological advances may occur to eliminate some of the fire and explosion risks of BESS but even if this happens, there is no requirement that the Applicant will install the newer safer versions in this BESS, while there is no compulsory obligation upon it to do so.

Professor Peter Dobson

12 April 2026

Particulates in Plumes from Lithium Ion Battery Fires.

There is more attention given to the emission of gases from lithium ion battery fires and this is to be welcomed from a health and safety point of view. However, less attention has been given to the particulates and aerosols in the smoke plume. Particulates are present in all fire plumes and these range in size from nanometre diameters to several micrometres. The most hazardous to human health are probably in the sum-micron range of < PM1.. These particles can affect both the pulmonary(lung) system and be rapidly absorbed into the brain via the olfactory and trigeminal nerves. This note is to highlight the evidence, so far, and to suggest that more attention should be given to collecting data as part of any safety assessment of a lithium ion Battery (BESS) installation.

Claassen et al (2024) (Appendix A) have given a very comprehensive account of the particulates to be found from fires of the two main battery types. Their paper identifies these and also states that the current preferred lithium ferrophosphate (LFP) type does emit more hydrofluoric acid and particles than the others. They also show that large quantities of the smaller < PM1 particles are emitted. It is these which are more dangerous to health and travel further.

The paper by Premnath et al (2025) (Appendix B) agrees with most of those findings, but they found that a higher number of particles were emitted from the Nickel Manganese Cobalt (NMC) cells. This might have been because of the state of charge of the battery cells. Premnath et al have shown that the state of charge is important and a highly charged battery emits more gas and particles when it fails by thermal runaway.

The fallout from the Moss Landing BESS fire in California in January 2025 (Appendix C) provides direct evidence of particulate contamination on soil several kilometres from the fire. Aiello et al (2025) give a detailed description of the early findings from this event. It should be noted that this

BESS used the older NMC cells and it was in a large old building which may have reduced the spread of particulates. This paper does highlight the challenges facing any collection of samples and data from such events. It also confirms the concern about fallout of particulates over larger distances than are often covered by diffusive modelling estimates.

Conclusion: It is very important that in the Risk Assessment for BESS that particulates are considered and identified. Developers and Planners should insist on using results of full-scale BESS fire tests to perform any modelling of the subsequent dispersion. Emphasis should be given to the presence of sub-micrometre particles because of the danger to health.

References

Aiello, I.W., et al., *Coastal wetland deposition of cathode metals from the world's largest lithium-ion battery fire.* Nature Scientific Reports, (2025). **15**(1): p. 42113 https://doi.org/10.1038/s41598-025-25972-8

Claassen, M., et al., *Characterization of Lithium-Ion Battery Fire Emissions—Part 2: Particle Size Distributions and Emission Factors.* Batteries, (2024). **10**(10): p. 366. https://doi.org/10.3390/batteries10100366

PremnathV et al *Characterization of particulate emissions from thermal runaway of lithium-ion cells.* ASME Journal of Electrochemical Energy Conversion and Storage. (2025) **22,** 031002-1 DOI: 10.1115/1.4065938

Professor Peter Dobson 14th April 2026.

batteries

MDPI

Article

Characterization of Lithium-Ion Battery Fire Emissions—Part 2: Particle Size Distributions and Emission Factors

[redacted]

[1] Division of Atmospheric Sciences, Desert Research Institute, Reno, NV 89512, USA; [redacted] (M.C.); [redacted] (B.B.); [redacted] (J.C.C.); [redacted] (J.G.W.)
[2] Department of Mechanical Engineering, University of Nevada, Reno, NV 89557, USA; [redacted]
[3] Atmospheric Sciences, Department of Physics, University of Nevada, Reno, NV 89557, USA
[4] Department of Mining and Metallurgical Engineering, University of Nevada, Reno, NV 89557, USA; [redacted]
* Correspondence: [redacted] Tel.: +[redacted]

Abstract: The lithium-ion battery (LIB) thermal runaway (TR) emits a wide size range of particles with diverse chemical compositions. When inhaled, these particles can cause serious adverse health effects. This study measured the size distributions of particles with diameters less than 10 µm released throughout the TR-driven combustion of cylindrical lithium iron phosphate (LFP) and pouch-style lithium cobalt oxide (LCO) LIB cells. The chemical composition of fine particles ($PM_{2.5}$) and some acidic gases were also characterized from filter samples. The emission factors of particle number and mass as well as chemical components were calculated. Particle number concentrations were dominated by those smaller than 500 nm with geometric number mean diameters below 130 nm. Mass concentrations were also dominated by smaller particles, with PM_1 particles making up 81–95% of the measured PM_{10} mass. A significant amount of organic and elemental carbon, phosphate, and fluoride was released as $PM_{2.5}$ constituents. The emission factor of gaseous hydrogen fluoride was 10–81 mg/Wh, posing the most immediate danger to human health. The tested LFP cells had higher emission factors of particles and HF than the LCO cells.

Keywords: Li-ion battery; fire; smoke; particulate matter; thermal runaway; ultrafine particles; HF; $PM_{2.5}$; emission factor; particle size distribution

check for updates

Citation: [redacted] Characterization of Lithium-Ion Battery Fire Emissions—Part 2: Particle Size Distributions and Emission Factors. *Batteries* **2024**, *10*, 366. https://doi.org/10.3390/batteries10100366

Academic Editor: [redacted]

Received: 24 August 2024
Revised: 17 September 2024
Accepted: 15 October 2024
Published: 16 October 2024

1. Introduction

Lithium-ion batteries (LIB) can generate significant gaseous and particulate emissions when they experience thermal failure, through venting, thermal runaway (TR), fire, and explosion [1,2]. The detailed characterization of particle size distribution (PSD), chemical composition, emission factor, temporal evolution, and thermal stability is important for LIB safety, including understanding the health effects of inhaled smoke particles, proper personal protection, the mechanisms of fire origination and propagation, fire detection and suppression, post-fire cleanup, and material recycling. For example, recent studies of soot particles from LIB fires show higher toxicity to human cells than wood smoke [3,4]. However, as shown in a recent review [2], few studies have examined particle emissions from LIB fires.

Size distribution is an important parameter that describes the transport behavior, atmospheric residence time, and inhalation risk of particles. LIB TR generates a wide range of particle sizes, varying from several nanometers to several millimeters. Most previous studies have focused on larger particles that settled in the combustion chamber after experiments. Zhang et al. [5] collected particles after burning a nickel manganese cobalt (NMC) LIB cell and separated them by sieving into four size fractions. The mass percentages were

44% for 0–0.85 mm, 36% for 0.85–1.70 mm, 9% for 1.70–2.00 mm, and 11% for 2.00–8.00 mm. Laser diffraction particle sizing showed that the volume distribution had a median diameter of 198 μm for the 0–0.85 mm size fraction. Several other studies focusing on larger particles also showed volume distribution median diameters >100 μm [6–8]. Due to their high temperature and large thermal mass, the larger sparking particles may contribute to igniting flammable gases and TR propagation [9]. As they dominate the emitted particle mass, the chemical composition of these larger particles provides useful information about particle origin and TR reactions [5,8,10]. When released into the environment, they may cause air, water, and soil contamination [11–13]. However, these particles represent a low inhalation risk to humans as their large size causes them to settle quickly by gravity and makes them unlikely to be inhaled while suspended in air [14].

Particles with aerodynamic diameters less than 10 μm (PM_{10}), 2.5 μm ($PM_{2.5}$), and even smaller (e.g., ultrafine particles with diameters <100 nm [$PM_{0.1}$]) can remain suspended in air for longer than larger particles. When inhaled, they will deposit at different locations in the human respiratory track depending on the particle size, causing respiratory, cardiovascular, and other diseases [15]. Very few studies have measured PM_{10} size distributions from LIB fires. Premnath et al. [16] used an Engine Exhaust Particle Sizer (EEPS) [17,18] to measure particle number concentrations in the size range of 5.6–560 nm in real time from lithium iron phosphate (LFP) and NMC cells undergoing TR. The geometric number mean diameters (GNMD) of the PSDs [19] ranged from 54 to 69 nm with either monomodal or bimodal distributions. The emission rate varied from 1.6×10^{15} to 2.1×10^{17} particles/hour, 5–6 orders of magnitude higher than modern heavy-duty diesel engines. While the tests evaluated the effects of the TR triggering mechanism (nail penetration vs. overcharging) and LIB chemistry (LFP vs. NMC), the number of tests were small, and the influence of the cell's state of charge (SOC) was not examined. Goupil et al. [20] measured PSDs from an NMC cell fire using a scanning mobility particle sizer (SMPS; 17.5–532.8 nm) and an optical particle spectrometer (250 nm–32 μm). The number distributions were bimodal, with one peak below 50 nm and one centered around 125 nm, while the mass distribution had a peak around 10 μm. The slow SMPS scan time (76 s) may cause inaccuracy in the PSD, and the conversion from optical to aerodynamic diameter is affected by the particle's optical properties, morphology, and density [21,22]. Several other studies have estimated PSDs from image analysis [2,11]. However, this method is prone to multiple artifacts, such as particle loss during collection and sample preparation, a compromise between field of view and size resolution, and potential overlaps between particles [23].

Emission factors (EFs) are commonly used in air quality management to estimate pollutant emissions based on emission activities [24]. Because the total emission amount depends on LIB SOCs and the number of LIBs burned, the proper activity metric for estimating LIB fire emissions is the total energy capacity of the LIB cells burned [25]. Therefore, the particle number EFs are expressed in particles/Wh (watt–hours), and the size-segregated PM mass and $PM_{2.5}$ constituent EFs are expressed in mg/Wh. EFs in these units are easier to use for estimating the total emissions than the emission rates in particles/hour reported by Premnath et al. [16]. To our knowledge, no studies have reported EFs of LIB fire particle chemical constituents.

In companion with the particle chemical characteristics presented by Claassen et al. [26], the objectives of this paper are to: (1) characterize the size distribution of particles in the diameter range of 6 nm–10 μm; (2) quantify the EFs of particle number, particle mass, and $PM_{2.5}$ constituents emitted from LIB combustion; and (3) evaluate the dependence of PSDs and EFs on cell type and SOC.

2. Materials and Methods

The experiments and data analysis have been described in the companion paper [26] and only a brief description is provided here. Two commonly used LIB types were tested: a cylindrical, 18650-style, LFP cell and a pouch-style lithium cobalt oxide (LCO) cell [27,28]. Each cell type was tested at five SOC levels with three to six tests per SOC. The cells used

for these tests were purchased shortly before the experimental campaign and were received at proper storage voltages. It was found that the LFP cells only vented at 0% and 30% SOCs, flamed at 50% and 75% SOCs, and had either venting or flaming at 100% SOCs. In contrast, LCO tests flamed at all SOCs [26]. While these two cell types will be referred to by their cell chemistry (LFP vs. LCO), they also differ in form-factor and casing, both of which can affect emissions. However, this study did not attempt to isolate the effects of these factors. The LIB combustion tests were conducted inside an ~8 m^3 burn chamber [29]. The exhaust flow rate (Q) was set to ~3300 L/min, as determined by thermal anemometer measurements in the exhaust duct [30]. Before each test, the chosen LIB cell was charged to the desired SOC by a programable charger. The cell was then placed in a ceramic crucible and heated to failure by an electric hot plate. A type K thermocouple was used to measure external cell and flame temperatures.

A sample of LIB combustion emissions was extracted from the chamber exhaust vent and directed to a suite of particle analyzers and the filter sampling system. Real-time particle mass concentrations were measured by two DustTrak DRX (TSI Inc., Shoreview, MN, USA) aerosol monitors in five size fractions (i.e., PM_1, $PM_{2.5}$, PM_4, PM_{10}, and PM_{15}) [21,22]. The DustTraks were placed before and after sample line dilution to determine the dilution factors.

Finer resolution PSDs in the range of 6 nm–10 µm were measured every second by an electrical low-pressure impactor (ELPI+; Dekati Ltd., Kangasala, Finland) [31–34] which was placed on a diluted sample line to prevent impactor overloading. In an ELPI+, particles are first introduced into a unipolar diffusion charger to achieve a stable charge distribution, and then are collected on 13 stages of electrically conducting cascade impactors and a final filter, depending on their aerodynamic diameters. The electrical charges carried by the deposited particles are measured as current by sensitive electrometers. An inversion algorithm is used to convert the 14-channel electric current data to particle number distributions with up to 500 bins. In this study, the particle number distributions were converted to mass distributions by assuming spherical particle shape and a density of 1 g/cm^3. The high-resolution data were integrated over the size fractions of <0.1 µm ($PM_{0.1}$), 0.1–1 µm ($PM_{0.1–1}$), 1–2.5 µm ($PM_{1–2.5}$), and 2.5–10 µm ($PM_{2.5–10}$). There are multiple potential artifacts (e.g., deposition of smaller particles at upper stages, size-dependent particle density, and image current) that could lead to errors in the mass concentration calculation [35]. Therefore, the ELPI $PM_{2.5}$ mass was normalized by gravimetric $PM_{2.5}$ mass to account for these artifacts.

Two filter channels were used to collect $PM_{2.5}$ and acidic gases for analysis of mass by gravimetry, ions and acidic gases by ion chromatography (IC), organic and elemental carbon (OC and EC) by thermal/optical analysis, and elements by x-ray fluorescence (XRF) and inductively coupled plasma mass spectrometry (ICP-MS) [24,36]. The backup potassium hydroxide (KOH)-impregnated cellulose-fiber filters behind the Teflon-membrane front filters were analyzed for acidic gases, including hydrogen fluoride (HF), hydrochloric acid (HCl), nitric acid (HNO_3), and sulfuric acid (H_2SO_4) as their corresponding ions (i.e., F^-, Cl^-, NO_3^-, and SO_4^{2-}) by IC [37,38].

Emission factors (EF_i in particles/Wh for particle number and mg/Wh for mass) were calculated for each species i by Equation (1):

$$EF_i = C_i \times Q \times \Delta t / E \quad (1)$$

where C_i (in particles/m^3 for number and mg/m^3 for mass) is the mean stack concentration for species i, Q (in m^3/s) is the mean stack exhaust flow rate, Δt (in s) is the sampling duration, and E (in Wh) is the nominal LIB cell energy capacity.

3. Results

3.1. Particle Size Distributions

Figure 1 shows the heat maps of PSD evolution for the representative tests for each cell type and SOC. The y-axis represents particle aerodynamic diameter (D_p), and the coloring

represents particle number concentration normalized by the size bin width (dlog (D_p)). While most particles had diameters below 500 nm, significant variations in PSD evolution were seen. Low SOC (0 and 30%) LFP tests in this study, which had no flaming combustion, emitted high concentrations of particles over a wide size range, but concentrations never exceeded 10^7 particles/cm^3. These emissions occurred for a long period of time, with maximum concentrations above 10^5 particles/cm^3 for over 30 min for both low SOCs.

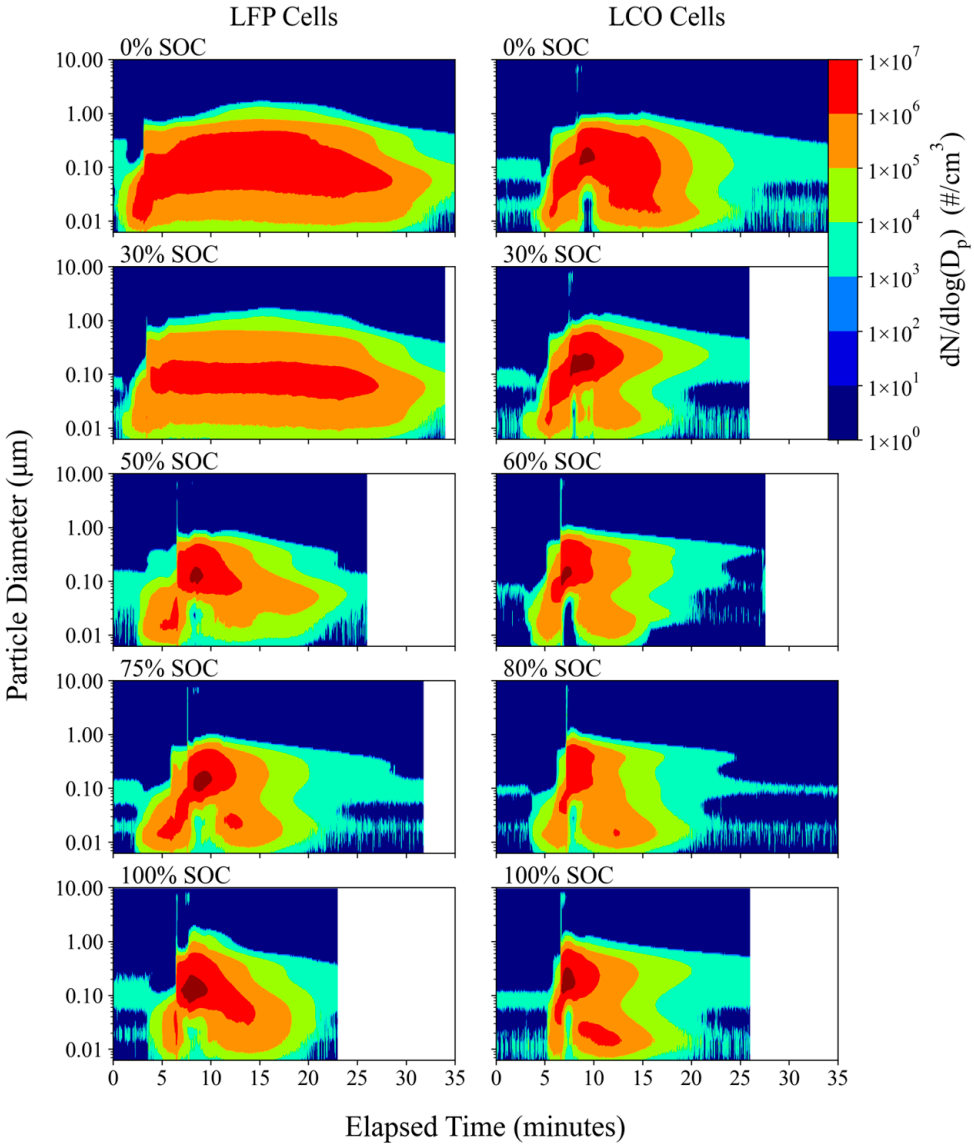

Figure 1. Particle number distribution heatmaps for representative LFP and LCO tests at each SOC.

Particle emissions for other LFP SOCs and LCO tests reached peak concentrations above 10^7 particles/cm^3, but concentrations above 10^5 particles/cm^3 only lasted for 10–18 min. A PSD discontinuity is seen in Figure 1 for these tests, occurring between five and ten minutes of elapsed time and representing abrupt concentration increases and particle size changes. This event coincided with visual and temperature-based TR indicators, suggesting it was caused by the onset of TR. A short 5–10 s long emission of coarse particles (up to 10 µm) can be seen to occur simultaneously, likely corresponding to the ejection of spark particles. Maximum particle concentrations occurred just after TR began. This is where most of the particle mass was emitted as particle sizes peaked here as well, with a notable decrease in particles below 50 nm in diameter. After this, peak

concentrations and particle sizes decreased gradually, often forming a bimodal pattern of nanoparticles (<100 nm) and larger particles between 100 nm and 1 µm.

Figures 2 and 3 show individual PSD "snapshots" for a 0% SOC LFP test and a 60% SOC LCO test, each at four time intervals. The 0% SOC LFP test only vented, without flaming combustion, while the 60% LCO test flamed vigorously. A detailed discussion of the observed combustion behavior for all tests can be found in [26]. The intervals include background concentrations (t_1), when the test cell is outgassing (t_2), after TR (t_3), and after combustion is complete and the test cell is smoldering (t_4). These time intervals were selected to represent similar combustion stages despite the differences in combustion duration between tests. The GNMDs and geometric number standard deviations (GNSD) were calculated to characterize the PSD at each time interval [19].

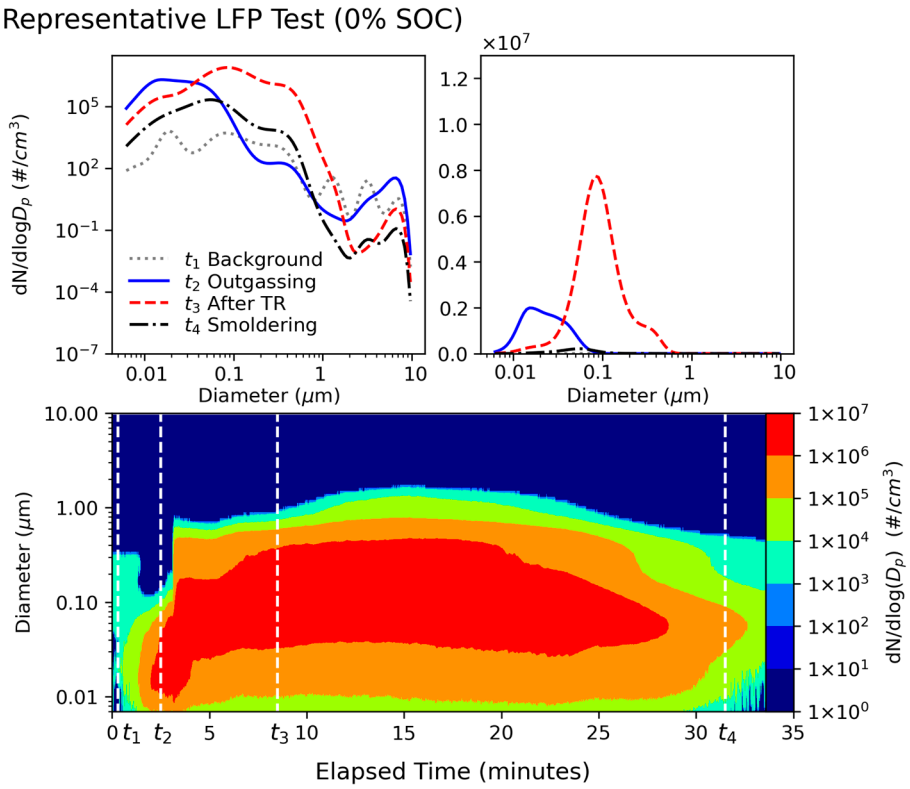

Figure 2. Particle number distribution snapshots (**left**: log scale and **right**: linear scale) and heatmap (**bottom**) for a representative 0% SOC LFP test. GNMDs for $t_{1–4}$ are 59 nm, 22 nm, 91 nm, and 49 nm, respectively.

The 0% SOC LFP "venting" test and the 60% SOC LCO "flaming" test had similar peak outgassing (t_2) concentrations at ~2×10^6 particles/cm^3 but the particle diameters were smaller for the venting test, with a GNMD of 22 nm and a GNSD of 1.7. The flaming outgassing concentrations peaked at 59 nm with a GNSD of 1.9. While different cell types are compared here, the intent is to contrast the PSD differences due to the varied combustion behavior of the tests, not to infer differences due to the cell type itself. Concentrations after TR (t_3) peaked at four and six times the outgassing concentration for the venting and flaming tests, respectively, with the flaming test PSD being generally larger-sized and narrower. GNMDs at this time were 91 nm and 195 nm for the venting and flaming tests, with GNSDs of 1.9 and 1.6, respectively.

Figure 4a,b show the evolution of PM_1, $PM_{2.5}$, and PM_{10} for the tests shown in Figures 2 and 3, respectively. PM_1 accounted for most of the emission mass. Large spikes of PM_{10} were observed at the onset of TR, corresponding to the emission of coarse particles ($PM_{2.5–10}$), as was discussed for Figure 1. Interestingly, small spikes of coarse particles also occurred just before TR and before $PM_{2.5}$ emissions began. This behavior may be

useful for early TR detection by LIB pack monitoring systems. The venting test (Figure 4a) shows $PM_{2.5}$ mass concentrations rising above PM_1 starting when emissions peaked around 15 min of elapsed time and lasting until combustion ended. This behavior occurred for all venting-only tests (LFP tests with 0% and 30% SOCs as well as half of the 100% SOC tests [26]). For tests where flaming occurred, PM_1 dominated PM mass emissions outside of TR onset.

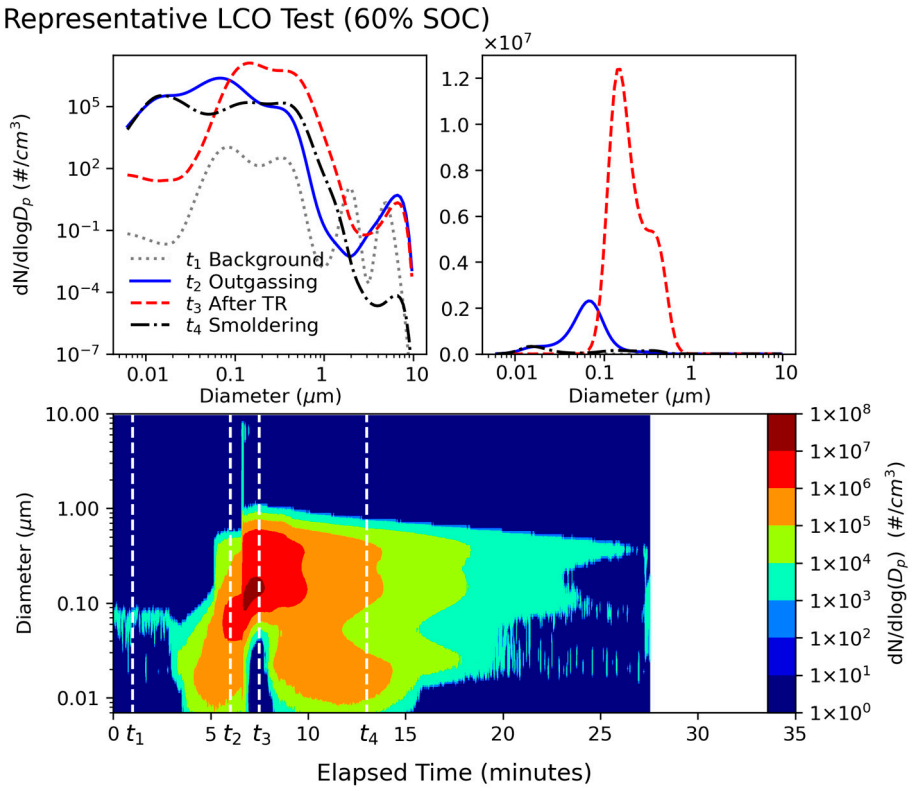

Figure 3. Particle number distribution snapshots (**left**: log scale and **right**: linear scale) and heatmap (**bottom**) for a representative 60% SOC LCO test. GNMDs for $t_{1–4}$ are 117 nm, 59 nm, 195 nm, and 52 nm, respectively.

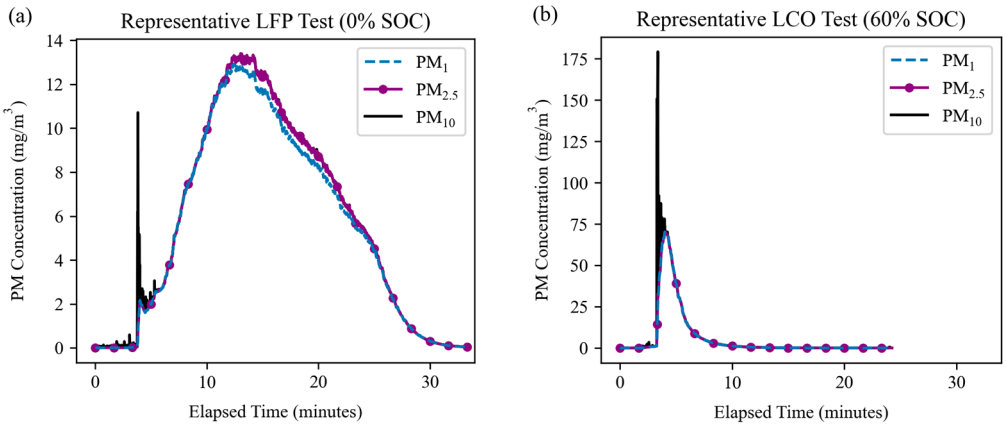

Figure 4. Mass concentrations of PM_1, $PM_{2.5}$, and PM_{10} for the representative tests: (**a**) LFP at 0% SOC and (**b**) LCO at 60% SOC (same as those in Figures 2 and 3). The coarse particles ($PM_{2.5–10}$) are released predominantly during TR.

Figure 5 shows the average number-based (a and b) and mass-based (c and d) PSDs for each SOC and cell type. The number distributions show a dominant mode centered around 70–140 nm, with additional modes centered around 20 nm and 300 nm. These

distributions are similar to those reported by Goupil et al. [20]. For LFP tests, particles were smaller and were released in lower concentrations at low SOCs, increasing in size and concentration at mid-SOCs. Tests with 100% SOC fell in the middle due to having disparate combustion behavior. This is consistent with the combustion behavior of LFP tests: they only vented at 0% and 30% SOCs, intensely flamed at 50% and 75% SOCs, and had more variable combustion at 100% SOCs [26]. Particle sizes also increased with SOC for LCO tests, but there was no consistent dependence of concentrations on SOC, likely because flaming combustion was observed at all SOCs. The mass distributions show that LFP tests with 0% and 30% SOCs only have one mode centered around 460 nm, with elevated concentrations between 1 and 2.5 µm. All other tests had bimodal distributions, with one fine-particle mode centered around 400 nm and a coarse-particle mode centered around 8 µm. This indicates that the coarse particles were generated from flaming rather than cell venting. The coarse particle mode mass increased with SOC for both cell types, being insignificant for low SOC LFP tests. The fine particle mode mass also increased with SOC for LFP tests as the PSD shifted to larger particle sizes. A coarse mode centered around 10 µm was also observed by Goupil et al. [20].

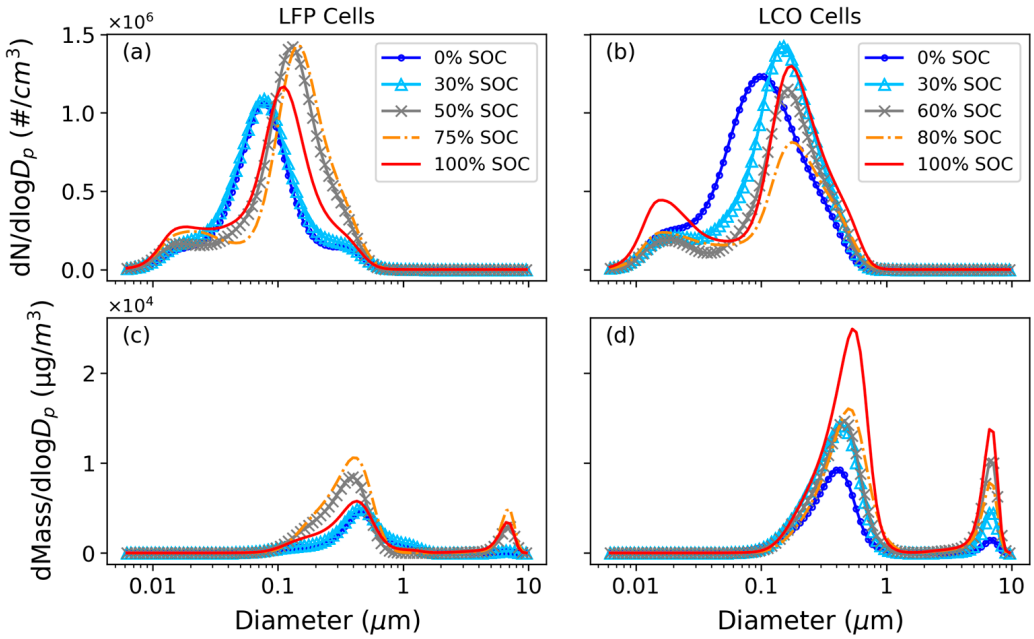

Figure 5. Particle number (top panels) and mass (bottom panels) distributions for LFP (**a**,**c**) and LCO (**b**,**d**) tests. An outlier was removed from some SOC groups to better show the prevailing trends.

Table 1 shows the GNMD and geometric mass mean diameters (GMMD) [19] for each cell type and SOC. The GNMD varied from 74 to 114 nm for LFP tests and 90 to 130 nm for LCO tests, showing that particles from LCO tests tended to be larger. GMMDs were larger than GNMDs due to mass being proportional to the cube of particle diameter. Interestingly, GNMDs peaked at mid-range SOCs while GMMDs increased with SOC, peaking at 100%. This increase at high SOCs, along with the previously discussed emission of large particles at TR, confirms that $PM_{2.5–10}$ is generated by the energetic combustion and ejection of material that occurs in a highly charged LIB cell during TR. Premnath et al. [16] found that GNMD and GMMD ranges were 54–69 nm and 97–204 nm for LFP and NMC cells, respectively, at 100% SOCs. These diameters are smaller than those in Table 1, especially for GMMD, which is likely caused by the lower upper size limit of the EEPS (560 nm) [17,18] than the ELPI+ (10 µm).

Table 1. Average and range (in parentheses) of geometric number mean diameters (GNMD) and geometric mass mean diameters (GMMD) for each SOC and cell type.

Cell Type	SOC (%)	GNMD (nm)	GMMD (nm)
LFP	0	74 (72–77)	415 (409–424)
	30	74 (72–77)	426 (403–453)
	50	110 (109–111)	425 (415–435)
	75	114 (106–129)	479 (434–530)
	100	84 (71–93)	568 (536–611)
LCO	0	90 (78–102)	387 (371–405)
	30	120 (111–137)	474 (470–477)
	60	130 (128–132)	663 (553–751)
	80	118 (109–128)	673 (651–704)
	100	116 (96–129)	668 (602–778)

3.2. Emission Factors (EFs)

EFs for particle number, mass, $PM_{2.5}$ constituents, and acidic gases are listed in Tables S1–S5. The following sections describe EFs for particle numbers, mass, carbon, PO_4^{3-}, selected metals and ions, and acidic gases, as well as the relationship between EF and combustion temperature.

3.2.1. EFs for Particle Number and Mass

Figure 6a shows particle number EFs by cell SOC for each size fraction. The EFs for ultrafine particles ($PM_{0.1}$) ranged between 1.5×10^{13} and 3.6×10^{13} particles/Wh for LFP tests and 3.2×10^{12} and 9.6×10^{12} particles/Wh for LCO tests (Table S1). Total particle numbers decreased with SOC, and LFP tests released several times more particles than LCO tests. $PM_{0.1}$ and $PM_{0.1–1}$ together accounted for >99.9% of PM_{10} numbers, at 42–84% and 16–58% of PM_{10}, respectively. Particles larger than 1 µm had negligible contributions to particle number. $PM_{0.1}$ tended to make up a higher proportion of PM_{10} when particle emissions were high. On the other hand, Figure 6b shows $PM_{0.1}$ made up a much smaller proportion of the PM_{10} mass due to having very small particle volumes, at 1–8%, while $PM_{0.1–1}$ dominated the PM_{10} mass at 77–89% due to their high concentrations. PM_1 particles made up 81–95% of the measured PM_{10} mass, as also shown in Figure 4. Larger particles made up significant portions of PM_{10} mass despite their low number concentrations, with $PM_{1–2.5}$ and $PM_{2.5–10}$ accounting for up to 4% and 18% of PM_{10} mass, respectively. $PM_{1–2.5}$ EFs were high for low SOC LFP tests and venting-only 100% SOC LFP tests while all other tests had higher $PM_{2.5–10}$ EFs instead.

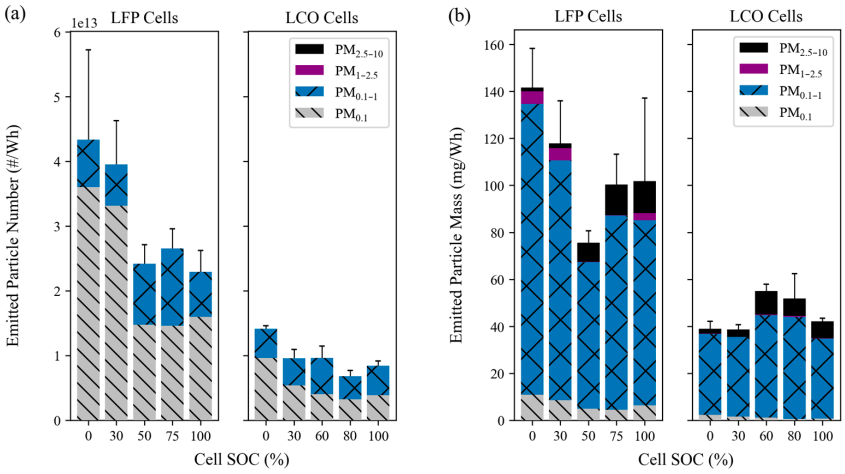

Figure 6. Emission factors for (**a**) particle number and (**b**) particle mass by size fraction for LFP and LCO tests. Error bars represent the total PM_{10} standard error (including all smaller particle sizes) and are symmetric.

3.2.2. EFs for $PM_{2.5}$, OC, EC, PO_4^{3-}, and Toxic Metals

EFs for $PM_{2.5}$, OC, EC, and PO_4^{3-} are shown in Figure 7a. EFs for $PM_{2.5}$ mass were between 35 and 140 mg/Wh. This equates to the emission of 1.4–5.6 g of $PM_{2.5}$ from the combustion of a standard laptop-sized LIB (40 Wh), or 2.1–8.4 kg of $PM_{2.5}$ from the combustion of an electric vehicle battery pack (60 kWh) if all cells are burned in a similar way as those in this study.

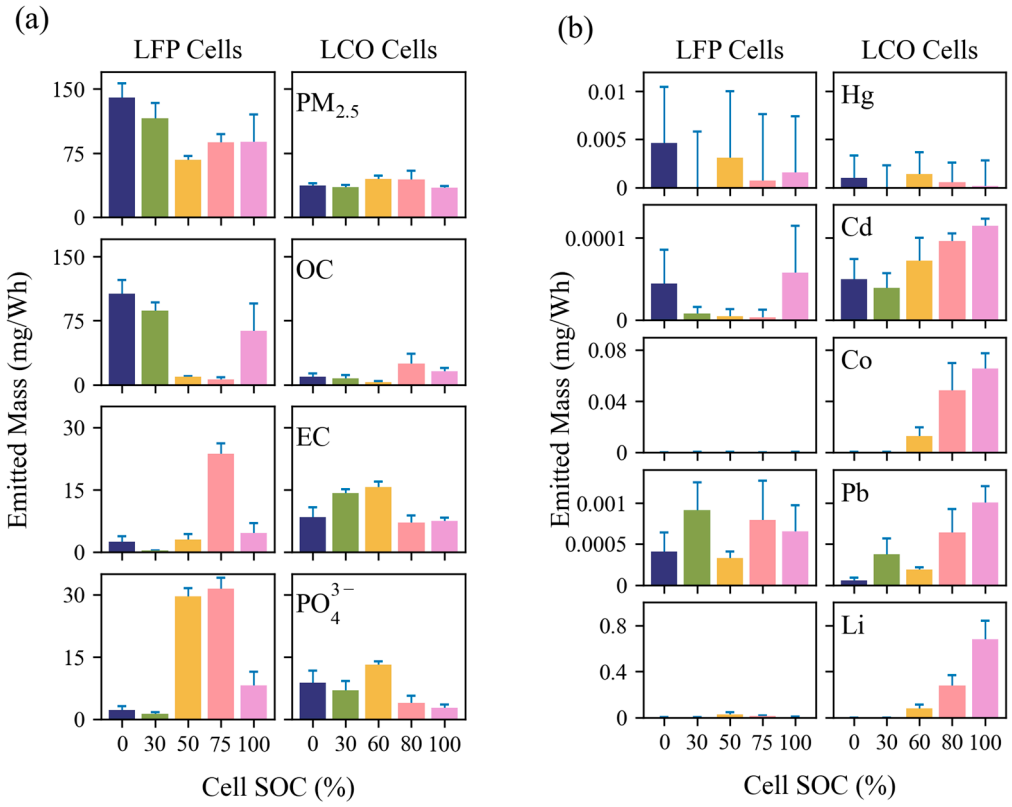

Figure 7. Emission factors for (**a**) $PM_{2.5}$ mass, OC, EC, and PO_4^{3-} and (**b**) selected metals. The error bars represent the larger of the propagated analytical uncertainty or the standard error within each SOC and are symmetric.

LFP tests had $PM_{2.5}$ EFs of 67–140 mg/Wh, with the least mass emitted at 50% SOC and increased variability at 100% SOC. OC EFs were 6–9 mg/Wh for 50–75% SOC and increased to 63–106 mg/Wh otherwise. OC variabilities at 100% SOC were similarly high to $PM_{2.5}$. Low OC emissions at mid-range SOCs corresponded to high EC emissions for 75% SOC only, where EC EFs spiked from <5 mg/Wh for all other SOCs to 24 mg/Wh. This resulted in total carbon EFs dropping from 109 mg/Wh (0% SOC) to 12 mg/Wh (50% SOC), before increasing back to 68 mg/Wh (100% SOC). PO_4^{3-} emissions were also significant for mid-range SOCs, at approximately 30 mg/Wh, but only 1–8 mg/Wh otherwise.

LCO tests had more consistent $PM_{2.5}$ mass EFs of 35–45 mg/Wh, lower than LFP tests by 1.5–3.8 times. EFs for OC, EC, and PO_4^{3-} had much less dependence on SOC for LCO tests than LFP tests. OC EFs were 3–24 mg/Wh and peaked at 75% SOC, where LFP OC was lowest. EC EFs were 7–16 mg/Wh, higher than those of LFP tests except for at 75%/80% SOC. PO_4^{3-} EFs were 3–13 mg/Wh with a similar SOC dependance to EC.

Figure 7b shows EFs for four hazardous air pollutant metals [39] and Li. Variability within SOCs was high but several features are notable. LCO tests had Cd, Co, Pb, and Li emissions that increase with SOC, reaching $(10 \pm 1) \times 10^{-5}$ mg/Wh for Cd, 0.07 ± 0.01 mg/Wh for Co, $(10 \pm 2) \times 10^{-4}$ mg/Wh for Pb, and 0.7 ± 0.2 mg/Wh for Li, all at 100% SOC. All of these elements were near detection limits at low SOCs except for Cd. Only Pb was consistently present for LFP tests at between $(30 \pm 8) \times 10^{-5}$ mg/Wh

and $(9 \pm 3) \times 10^{-4}$ mg/Wh, with no dependence on SOC. Hg and Cd were detected sporadically. EFs for major compositions and elements are summarized in Tables S2 and S5, respectively.

3.2.3. EFs for Anions and Acidic Gases

EFs for acidic gases HF, HCl, HNO_3, and H_2SO_4 and their corresponding particulate anions are shown in Figure 8. These acidic gases are toxic and corrosive and can cause adverse effects on human health and material integrity if not neutralized after emission.

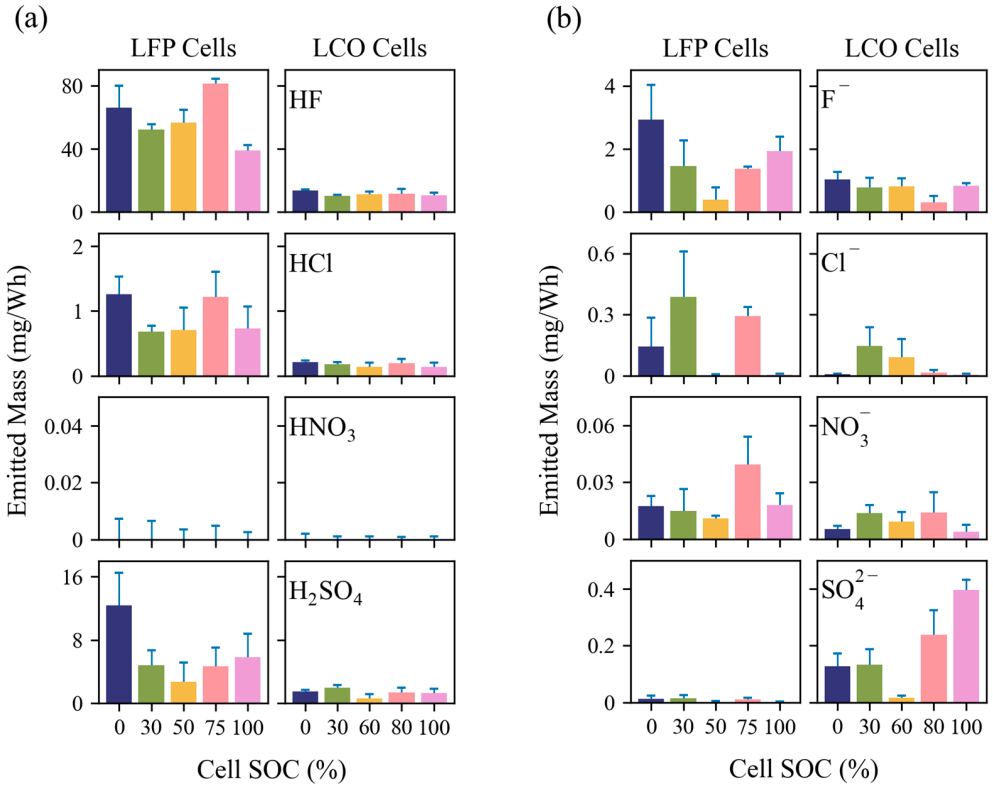

Figure 8. Emission factors for (**a**) selected acidic gases and (**b**) corresponding particulate anions. The error bars represent the larger of the propagated analytical uncertainty or the standard error within each SOC and are symmetric.

Gaseous EFs were higher than that of particulate emissions (by cell type) for all compounds shown except for NO_3^-, where HNO_3 emission was not detected. Gaseous HF and particulate F^- had the highest EFs for all LIB types and SOCs. Gaseous HF EFs ranged from 39 to 81 mg/Wh for LFP tests and 10 to 14 mg/Wh for LCO tests. Neither cell type showed a relationship between SOC and HF emissions. Particulate F^- EFs ranged from 0.4 to 3 mg/Wh for LFP tests and 0.3 to 1 mg/Wh for LCO tests. Particulate F^- had a distinct minimum at 50% SOC for LFP tests, corresponding to the minimum $PM_{2.5}$ EF (Figure 7a). Gaseous H_2SO_4 was the second most emitted acidic compound, with much higher gaseous emissions than particulate. Gaseous EFs were 3–12 mg/Wh for LFP tests and 0.6–2 mg/Wh for LCO tests. Unlike gaseous H_2SO_4 and all other acidic emissions shown, particulate SO_4^{2-} emissions were much higher for LCO tests than LFP tests, where only trace concentrations were detected. LCO tests had EFs of 0.1–0.4 mg/Wh for most SOCs, but only trace amounts for 60% SOC. Both gaseous and particulate emissions were low for 50/60% SOC, but this was more pronounced for LFP tests. Particle SO_4^{2-} emissions for LCO tests increased with SOC with the exception of 60% SOC. Gaseous HCl was consistently detected, averaging 0.9 mg/Wh for LFP tests and 0.2 mg/Wh for LCO tests. Particulate Cl^- was present sporadically for both cell types with EFs of up to 0.4 mg/Wh.

Only particulate NO_3^- was detected at between 0.005 and 0.04 mg/Wh, with higher emissions from LFP tests.

Table 2 compares the gaseous EFs of HF and HCl with the values reported in the literature. LFP HF emissions in this study (39–81 mg/Wh) compared well with the literature values which range at 12–350 mg/Wh. Emissions from LCO tests (10–14 mg/Wh) were lower than the 30–40 mg/Wh found in the literature, but this may be due to the limited number of studies [25,40]. Other cell types were reported to release a comparable 1–200 mg/Wh of HF. HCl emissions were reported by Diaz et al. [40] at 8–125 mg/Wh for LFP and LCO cells, significantly higher than those measured in this study (0.1–1.3 mg/Wh). No published EF values for HNO_3 or H_2SO_4 were found. Acidic gas and particulate ion EFs for all cell types and SOCs are listed in Tables S3 and S4, respectively.

Table 2. Comparison of gaseous emissions of HF and HCl to the literature sources, grouped by cell chemistry. EFs for HNO_3 and H_2SO_4 were not found in the literature.

Source	Cell Type	HF (mg/Wh)	HCl (mg/Wh)
This study	LFP	39–81	0.7–1.3
[40]	LFP	350	125
[25]	LFP	12–24	
[41]	LFP	40–125	
This study	LCO	10–14	0.14–0.21
[40]	LCO	30	8
[25]	LCO	30–40	
[42]	Unknown	20–200	
[43]	LMO	40–70	
[44]	NMC/LFP	23–36	
[45]	NMC	1–10	
[46]	NMC	4.2	

3.2.4. Relationship between Emission Factors and Combustion Temperatures

Figure 9 shows the relationship between the EF and the maximum measured combustion temperature for LFP tests. Cell SOC is also labeled by symbol coloring to show groupings. With the exception of two outlier tests (Tests C1 and C8 in Figure 9a,b), EFs for $PM_{2.5}$ and OC were found to decrease with increasing combustion temperature. This is expected as higher temperatures indicate more complete combustion that will release more gaseous CO_2 instead of carbonaceous particulate. In contrast, PO_4^{3-} increased with combustion temperatures, indicating more efficient conversion of P-containing electrolyte and cathode materials to particle emissions. Low EC emissions were found at lower combustion temperatures as expected; however, EC was not necessarily higher at high temperatures. Figure 9c shows that the 50% SOC tests had temperatures >600 °C but the EC emissions were comparable to those of low temperature tests. Particulate F^- and gaseous HF (Figure 9e,h) had the opposite trend, with F^- decreasing (for SOCs > 30%) and HF increasing with increasing temperature. This is possibly due to more HF remaining in the gas phase at higher temperatures rather than condensing to form particles. Li^+ emissions were hardly detected below 600 °C and increased rapidly thereafter, indicating a potential exponential relationship. More tests with temperatures reaching >700 °C are needed to explore this. Figure 9g shows that the part of $PM_{2.5}$ mass with unidentified composition increased with temperature, a correlation that could help determine what additional components (e.g., unmeasured phosphorous compounds) [26] need to be analyzed for.

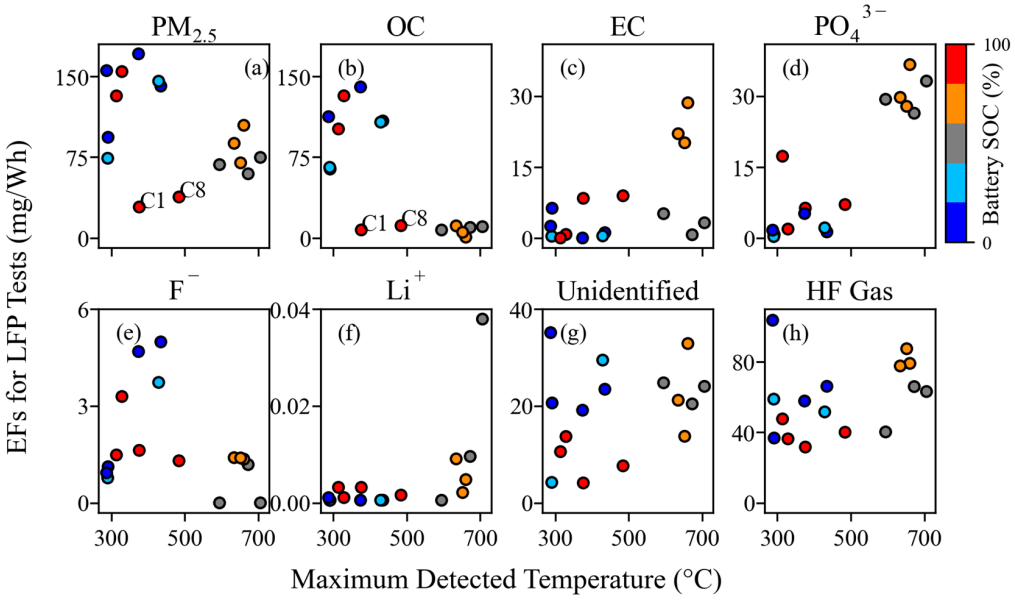

Figure 9. Relationship between EFs and maximum detected combustion temperature for LFP tests. LCO tests showed little correlation, possibly due to poor temperature measurement, and are not shown.

3.3. Cell Mass Losses

Each cell was weighed before and after combustion to determine the cell mass that was lost. LFP cells lost 2.2–2.4 g/Wh during combustion for all except 50% SOC, which lost noticeably less at 1.8–2 g/Wh. LCO cells lost roughly half the mass per Wh of cell capacity at 0.95–1.2 g/Wh. As shown in Table S6, this equates to a loss of ~20% of the cell mass for both cell types. However, only approximately 0.6–1.2% of the total cell mass, or 3–6% of the lost cell mass, was emitted as $PM_{2.5}$ that reached the filter assemblies. The proportion of lost cell mass that was emitted as $PM_{2.5}$ was highest for low SOC LFP tests, where 5–6% was converted to $PM_{2.5}$. All other SOC groups averaged 3–4%. By subtraction, this means that 94–97% of the lost mass, or roughly 16–22% of total cell mass, was emitted as either settleable PM or as gas emissions. As shown in Table S6, cell mass losses from previous studies range from 15% to 60%, with settleable particle mass accounting for 5–50% of the original cell mass, depending on the cell chemistry, casing, and SOCs [5,6,10,47]. Even though $PM_{2.5}$ only accounted for a small fraction of the total PM mass emitted from LIB fires, it accounts for most of the particle numbers that can be inhaled by humans and presents great health risks.

4. Discussion and Conclusions

This study conducted a detailed characterization of the size distribution of particles with diameter less than 10 μm emitted from LIB fires and determined EFs for size-segregated particle number, particle mass, and $PM_{2.5}$ chemical constituents. The analysis covered two cell types at a range of SOCs. While emissions may vary significantly depending on the specific cell types or LIB pack sizes, the cells tested represent two common cell chemistries and form-factors, in terms of both cell construction and energy capacity, that are used widely in modern LIB applications. As such, the findings offer valuable insights into the characteristics of emission from LIB combustion. The key conclusions are as follows:

(1) LIB fires emit high concentrations of fine and ultrafine particles. The particle number distributions showed a dominant mode centered around 100 nm, with additional modes centered around 20 nm and 300 nm. The particle mass distributions showed that the venting-only LFP tests in this study with 0% and 30% SOCs had one mode centered around 460 nm, while all other tests had bimodal distributions, with one fine particle mode centered around 400 nm and a coarse particle mode centered

around 8 μm. $PM_{0.1}$ and $PM_{0.1–1}$ together accounted for >99.9% of PM_{10} numbers, while $PM_{0.1–1}$ dominated the PM_{10} mass at 77–89%. Super-micron particles have non-negligible mass contributions, with $PM_{1–2.5}$ and $PM_{2.5–10}$ accounting for up to 4% and 18% of PM_{10} mass, respectively. $PM_{1–2.5}$ was emitted during cell venting, after TR and when flaming did not occur, while $PM_{2.5–10}$ was emitted just before and during TR onset for all tests.

(2) Venting-only combustion (LFP tests at 0% SOC, 30% SOC, and some at 100% SOC) showed smooth evolution of PSDs, while the onset of TR caused a discontinuity in particle size distribution by increasing both mode diameter and concentration and releasing coarse mode particles (1–10 μm). Particles from LCO tests in this study (GNMD 90–130 nm; GMMD 387–673 nm) were generally larger than those from LFP tests (GNMD 74–114 nm; GMMD 415–568 nm). The GMMD increased with SOC.

(3) LFP tests had higher EFs for particle number and mass than LCO tests. The EFs for ultrafine particles ($PM_{0.1}$) ranged from 1.5×10^{13} to 3.6×10^{13} particles/Wh for LFP and 3.2×10^{12} to 9.6×10^{12} particles/Wh for LCO tests. LFP tests had $PM_{2.5}$ EFs between 67 and 140 mg/Wh with more variability at different SOCs, whereas LCO tests had lower and more consistent $PM_{2.5}$ mass EFs between 35 and 45 mg/Wh. Even though $PM_{2.5}$ only accounted for 0.25–1.5% of the total cell mass and a small fraction of total PM mass emitted from LIB fires, it accounts for the most particle numbers that can be inhaled by humans and presents great health risks.

(4) LIB fires emit acidic gases, such as HF, HCl, and H_2SO_4. Gaseous HF ranged from 39 to 81 mg/Wh for LFP tests and 10 to 14 mg/Wh for LCO tests. These toxic and corrosive gases may represent great hazards to people and properties.

(5) Emissions are highly dependent on cell type, SOC, and combustion temperatures. The emitted $PM_{2.5}$ mass can depend on cell SOC by a factor of two, while the emitted OC, EC, and PO_4^{3-} can differ by a factor of 10 or more. PO_4^{3-} increased with combustion temperature, particularly when it reached >500 °C. Toxic metal emissions increased with SOC, but only for LCO tests, with no trend for LFP tests. Acidic gas emissions depended primarily on cell type, indicating that cell design is crucial to lowering emissions of HF and other corrosive compounds. The emission dependence on LIB cell properties should be considered when evaluating the overall hazard that each LIB pack presents. For example, while LFP cells are known to be more thermally stable, results from this study show that they may release more HF and can generate higher particulate concentrations than LCO cells.

The emissions documented here have implications for health and safety as well as environmental contamination. Considering that modern LIB packs can contain hundreds to millions of Wh of energy capacity, the effects of significant emissions of volatile organics, ultrafine and fine particles, hazardous metals, and acidic compounds must be taken into consideration when responding to and cleaning up after LIB fires.

LIB fires are becoming more common as LIB use expands. The combustion process can occur quickly and without warning, limiting the effectiveness of fire suppression. Therefore, a detailed understanding of the resulting emissions is imperative to allow for effective fire response and cleanup. This paper has detailed the expected fine particulate emissions in a way that allows extrapolation to any size LIB pack if the burned LIB energy capacity is known. This resource will allow first responders, LIB manufacturers, and responsible authorities to plan for and respond to LIB fires.

Supplementary Materials: The following supporting information can be downloaded at: https://www.mdpi.com/article/10.3390/batteries10100366/s1, Table S1. EFs for four size fractions in particles/Wh and mg/Wh for particle number and particle mass, respectively; Table S2. EFs in mg/Wh for $PM_{2.5}$ chemical constituents; Table S3. EFs in mg/Wh for acidic gases for all cell types and SOCs; Table S4. EFs in mg/Wh for particulate anions and cations for all cell types and SOCs; Table S5. EFs in mg/Wh for elements for all cell types and SOCs; Table S6. A comparison of cell mass loss rates to the literature values [5,6,10,47].

Author Contributions: Conceptualization, X.W.; Methodology, M.C. and X.W.; Software, M.C.; Validation, M.C. and X.W.; Formal Analysis, M.C.; Investigation, M.C., B.B., and X.W.; Resources, X.W.; Data Curation, M.C.; Writing—Original Draft Preparation, M.C. and X.W.; Writing—Review and Editing, X.W., J.C.C., J.G.W., P.C., and Y.W.; Visualization, M.C.; Supervision, X.W. and Y.W.; Project Administration, X.W.; Funding Acquisition, X.W. All authors have read and agreed to the published version of the manuscript.

Funding: This research was funded by the U.S. National Aeronautics and Space Administration's Established Program to Stimulate Competitive Research, CAN Grant No. 80NSSC19M0152, and Nevada Space Grant No. 80NSSC20M0043 22–24.

Data Availability Statement: The raw data supporting the conclusions of this article will be made available by the authors on request. The calculated emission factors for all measured species are included in the Supplementary Materials.

Acknowledgments: The authors thank Hans Moosmüller for the use of the burn chamber where experiments were performed and DRI personnel for support and filter analysis.

Conflicts of Interest: The authors declare no conflicts of interest.

Abbreviations

Δt	sampling duration
C	concentration
Cd	cadmium
Cl^-	chloride
Co	cobalt
D_p	particle diameter
E	battery cell energy capacity
EC	elemental carbon
EEPS	engine exhaust particle sizer
EF	emission factor
ELPI	electrical low-pressure impactor
F^-	fluoride
GMMD	geometric mass mean diameter: mean diameter of a particle mass distribution in logarithmic scale
GNMD	geometric number mean diameter: mean diameter of a particle number distribution in logarithmic scale
GNSD	geometric number standard deviation: standard deviation of a particle number distribution in logarithmic scale
HCl	hydrochloric acid
Hg	mercury
HF	hydrofluoric acid
HNO_3	nitric acid
H_2SO_4	sulfuric acid
IC	ion chromatography
ICP-MS	inductively coupled plasma mass spectrometry
KOH	potassium hydroxide
LCO	lithium cobalt oxide
Li	lithium
Li^+	lithium ion
LIB	lithium-ion battery
LFP	lithium iron phosphate
NMC	nickel manganese cobalt
NO_3^-	nitrate
OC	organic carbon
P	phosphorus
Pb	lead
PM	particulate matter
PM_x	particles with aerodynamic diameters $\leq$x μm

PO_4^{3-}	phosphate
PSD	particle size distribution
Q	flow rate
SMPS	scanning mobility particle sizer
SO_4^{2-}	sulfate
SOC	state of charge
TR	thermal runaway
Wh	watt hours
XRF	X-ray fluorescence

References

1. Bugryniec, P.J.; Resendiz, E.G.; Nwophoke, S.M.; Khanna, S.; James, C.; Brown, S.F. Review of gas emissions from lithium-ion battery thermal runaway failure—Considering toxic and flammable compounds. *J. Energy Storage* **2024**, *87*, 111288. [CrossRef]
2. Li, W.; Xue, Y.; Feng, X.; Rao, S.; Zhang, T.; Gao, Z.; Guo, Y.; Zhou, H.; Zhao, H.; Song, Z.; et al. Characteristics of particle emissions from lithium-ion batteries during thermal runaway: A review. *J. Energy Storage* **2024**, *78*, 109980. [CrossRef]
3. Xu, Y.; Wang, Y.; Chen, X.; Pang, K.; Deng, B.; Han, Z.; Shao, J.; Qian, K.; Chen, D. Thermal runaway and soot production of lithium-ion batteries: Implications for safety and environmental concerns. *Appl. Therm. Eng.* **2024**, *248*, 123193. [CrossRef]
4. Xu, Y.; Wang, Y.; Chen, D. Soot formation and its hazards in battery thermal runaway. *J. Aerosol Sci.* **2024**, *181*, 106420. [CrossRef]
5. Zhang, Y.; Wang, H.; Li, W.; Li, C.; Ouyang, M. Size distribution and elemental composition of vent particles from abused prismatic Ni-rich automotive lithium-ion batteries. *J. Energy Storage* **2019**, *26*, 100991. [CrossRef]
6. Zhang, Y.; Wang, H.; Li, W.; Li, C. Quantitative identification of emissions from abused prismatic Ni-rich lithium-ion batteries. *eTransportation* **2019**, *2*, 100031. [CrossRef]
7. Wang, H.; Zhang, Y.; Li, W.; Li, C.; Ouyang, M. Particles released by abused prismatic Ni-rich automotive lithium-ion batteries. *WSEAS Trans. Syst. Control* **2020**, *15*, 30–38. [CrossRef]
8. Wang, H.; Wang, Q.; Jin, C.; Xu, C.; Zhao, Y.; Li, Y.; Zhong, C.; Feng, X. Detailed characterization of particle emissions due to thermal failure of batteries with different cathodes. *J. Hazard. Mater.* **2023**, *458*, 131646. [CrossRef]
9. Wang, G.; Kong, D.; Ping, P.; Wen, J.; He, X.; Zhao, H.; He, X.; Peng, R.; Zhang, Y.; Dai, X. Revealing particle venting of lithium-ion batteries during thermal runaway: A multi-scale model toward multiphase process. *eTransportation* **2023**, *16*, 100237. [CrossRef]
10. Essl, C.; Golubkov, A.W.; Gasser, E.; Nachtnebel, M.; Zankel, A.; Ewert, E.; Fuchs, A. Comprehensive Hazard Analysis of Failing Automotive Lithium-Ion Batteries in Overtemperature Experiments. *Batteries* **2020**, *6*, 30. [CrossRef]
11. Yang, Y.; Fang, D.; Maleki, A.; Kohzadi, S.; Liu, Y.; Chen, Y.; Liu, R.; Gao, G.; Zhi, J. Characterization of Thermal-Runaway Particles from Lithium Nickel Manganese Cobalt Oxide Batteries and Their Biotoxicity Analysis. *ACS Appl. Energy Mater.* **2021**, *4*, 10713–10720. [CrossRef]
12. Held, M.; Tuchschmid, M.; Zennegg, M.; Figi, R.; Schreiner, C.; Mellert, L.D.; Welte, U.; Kompatscher, M.; Hermann, M.; Nachef, L. Thermal runaway and fire of electric vehicle lithium-ion battery and contamination of infrastructure facility. *Renew. Sustain. Energy Rev.* **2022**, *165*, 112474. [CrossRef]
13. Bordes, A.; Papin, A.; Marlair, G.; Claude, T.; El-Masri, A.; Durussel, T.; Bertrand, J.-P.; Truchot, B.; Lecocq, A. Assessment of Run-Off Waters Resulting from Lithium-Ion Battery Fire-Fighting Operations. *Batteries* **2024**, *10*, 118. [CrossRef]
14. ICRP. Human Respiratory Tract Model for Radiological Protection. ICRP Publication 66. Ann. ICRP 24 (1-3). 1994. Available online: https://www.icrp.org/publication.asp?id=icrp%20publication%2066 (accessed on 2 July 2024).
15. Thangavel, P.; Park, D.; Lee, Y.C. Recent Insights into Particulate Matter (PM(2.5))-Mediated Toxicity in Humans: An Overview. *Int. J. Env. Res. Public Health* **2022**, *19*, 7511. [CrossRef] [PubMed]
16. Premnath, V.; Wang, Y.; Wright, N.; Khalek, I.; Uribe, S. Detailed characterization of particle emissions from battery fires. *Aerosol Sci. Technol.* **2022**, *56*, 337–354. [CrossRef]
17. Wang, X.L.; Grose, M.A.; Avenido, A.; Stolzenburg, M.R.; Caldow, R.; Osmondson, B.L.; Chow, J.C.; Watson, J.G. Improvement of Engine Exhaust Particle Sizer (EEPS) size distribution measurement—I. Algorithm and applications to compact-shape particles. *J. Aerosol Sci.* **2016**, *92*, 95–108. [CrossRef]
18. Wang, X.L.; Grose, M.A.; Caldow, R.; Osmondson, B.L.; Swanson, J.J.; Chow, J.C.; Watson, J.G.; Kittelson, D.B.; Li, Y.; Xue, J.; et al. Improvement of Engine Exhaust Particle Sizer (EEPS) size distribution measurement—II. Engine exhaust particles. *J. Aerosol Sci.* **2016**, *92*, 83–94. [CrossRef]
19. Hinds, W.C. *Aerosol Technology, Properties, Behavior, and Measurement of Airborne Particles*, 2nd ed.; Wiley: Los Angeles, CA, USA, 1999.
20. Goupil, V.; Gaya, C.; Boisard, A.; Robert, E. Effect of the heating rate on the degassing and combustion of cylindrical Li-Ion cells. *Fire Saf. J.* **2022**, *133*, 103648. [CrossRef]
21. Wang, X.L.; Chancellor, G.; Evenstad, J.; Farnsworth, J.E.; Hase, A.; Olson, G.M.; Sreenath, A.; Agarwal, J.K. A Novel Optical Instrument for Estimating Size Segregated Aerosol Mass Concentration in Real Time. *Aerosol Sci. Technol.* **2009**, *43*, 939–950. [CrossRef]

22. Wang, X.L.; Zhou, H.; Arnott, W.P.; Meyer, M.E.; Taylor, S.; Firouzkouhi, H.; Moosmüller, H.; Chow, J.C.; Watson, J.G. Evaluation of gas and particle sensors for detecting spacecraft-relevant fire emissions. *Fire Saf. J.* **2020**, *113*, 102977. [CrossRef]
23. Lee, J.; He, S.; Song, G.; Hogan, C.J. Size distribution monitoring for chemical mechanical polishing slurries: An intercomparison of electron microscopy, dynamic light scattering, and differential mobility analysis. *Powder Technol.* **2022**, *396*, 395–405. [CrossRef]
24. Wang, X.L.; Firouzkouhi, H.; Chow, J.C.; Watson, J.G.; Carter, W.; De Vos, A.S. Characterization of gas and particle emissions from open burning of household solid waste from South Africa. *Atmos. Chem. Phys.* **2023**, *23*, 8921–8937. [CrossRef]
25. Larsson, F.; Andersson, P.; Blomqvist, P.; Mellander, B.-E. Toxic fluoride gas emissions from lithium-ion battery fires. *Sci. Rep.* **2017**, *7*, 10018. [CrossRef] [PubMed]
26. Claassen, M.; Bingham, B.; Chow, J.C.; Watson, J.G.; Wang, Y.; Wang, X. Characterization of Lithium-Ion Battery Fire Emissions—Part 1: Chemical Composition of Fine Particles (PM2. 5). *Batteries* **2024**, *10*, 301. [CrossRef]
27. Lithiumwerks. APR18650M1B Nanophosphate® Technology Data Sheet. Austin, Texas. 2023. Available online: https://lithiumwerks.com/products/lithium-ion-18650-cells/ (accessed on 2 July 2024).
28. AA Portable Power Corp. Model 544792 Polymer Lithium-Ion Battery Data Sheet. Available online: https://www.batteryspace.com/prod-specs/3175.pdf (accessed on 2 July 2024).
29. Tian, J.; Chow, J.C.; Cao, J.; Han, Y.; Ni, H.; Chen, L.-W.A.; Wang, X.; Huang, R.; Moosmu, H.; Watson, J.G. A biomass combustion chamber: Design, evaluation, and a case study of wheat straw combustion emission tests. *Aerosol Air Qual. Res.* **2015**, *15*, 2104–2114. [CrossRef]
30. U.S. EPA. Method 1—Sample and Velocity Traverses for Stationary Sources. Code of Federal Regulations, Title 40, Part 60, Appendix A-1. Available online: https://www.ecfr.gov/current/title-40/chapter-I/subchapter-C/part-60/appendix-Appendix%20A-1%20to%20Part%2060 (accessed on 6 August 2024).
31. Järvinen, A.; Aitomaa, M.; Rostedt, A.; Keskinen, J.; Yli-Ojanperä, J. Calibration of the new electrical low pressure impactor (ELPI+). *J. Aerosol Sci.* **2014**, *69*, 150–159. [CrossRef]
32. Saari, S.; Arffman, A.; Harra, J.; Rönkkö, T.; Keskinen, J. Performance evaluation of the HR-ELPI+ inversion. *Aerosol Sci. Technol.* **2018**, *52*, 1037–1047. [CrossRef]
33. Marjamäki, M.; Keskinen, J.; Chen, D.-R.; Pui, D.Y.H. Performance Evaluation of the Electrical Low-Pressure Impactor (ELPI). *J. Aerosol Sci.* **2000**, *31*, 249–261. [CrossRef]
34. Keskinen, J.; Pietarinen, K.; Lehtimäki, M. Electrical low pressure impactor. *J. Aerosol Sci.* **1992**, *23*, 353–360. [CrossRef]
35. Maricq, M.M.; Podsiadlik, D.H.; Chase, R.E. Size Distributions of Motor Vehicle Exhaust PM: A Comparison Between ELPI and SMPS Measurements. *Aerosol Sci. Technol.* **2000**, *33*, 239–260. [CrossRef]
36. Wang, X.; Firouzkouhi, H.; Chow, J.C.; Watson, J.G.; Ho, S.S.H.; Carter, W.; De Vos, A.S. Chemically speciated air pollutant emissions from open burning of household solid waste from South Africa. *Atmos. Chem. Phys.* **2023**, *23*, 15375–15393. [CrossRef]
37. Eldering, A.; Solomon, P.A.; Salmon, L.G.; Fall, T.; Cass, G.R. Hydrochloric acid: A regional perspective on concentrations and formation in the atmosphere of Southern California. *Atmos. Environ. Part A Gen. Top.* **1991**, *25*, 2091–2102. [CrossRef]
38. Sturges, W.T.; Harrison, R.M. The use of nylon filters to collect HCl: Efficiencies, interferences and ambient concentrations. *Atmos. Environ. (1967)* **1989**, *23*, 1987–1996. [CrossRef]
39. U.S. EPA. *Initial List of Hazardous Air Pollutants with Modifications*; Air Toxics Assessment Group, U.S. Environmental Protection Agency: Research Triangle Park, NC, USA, 2020. Available online: https://www.epa.gov/haps/initial-list-hazardous-air-pollutants-modifications (accessed on 6 August 2024).
40. Diaz, F.; Wang, Y.; Weyhe, R.; Friedrich, B. Gas generation measurement and evaluation during mechanical processing and thermal treatment of spent Li-ion batteries. *Waste Manag.* **2019**, *84*, 102–111. [CrossRef]
41. Andersson, P.; Blomqvist, P.; Lorén, A.; Larsson, F. *Investigation of Fire Emissions from Li-Ion Batteries*; SP Technical Research Institute of Sweden: Borås, Sweden, 2013.
42. Larsson, F. *Lithium-Ion Battery Safety-Assessment by Abuse Testing, Fluoride Gas Emissions and Fire Propagation*; Chalmers Tekniska Hogskola: Göteborg, Sweden, 2017.
43. Ribière, P.; Grugeon, S.; Morcrette, M.; Boyanov, S.; Laruelle, S.; Marlair, G. Investigation on the fire-induced hazards of Li-ion battery cells by fire calorimetry. *Energy Environ. Sci.* **2012**, *5*, 5271–5280. [CrossRef]
44. Sturk, D.; Rosell, L.; Blomqvist, P.; Ahlberg Tidblad, A. Analysis of li-ion battery gases vented in an inert atmosphere thermal test chamber. *Batteries* **2019**, *5*, 61. [CrossRef]
45. Bordes, A.; Marlair, G.; Zantman, A.; Herreyre, S.; Papin, A.; Desprez, P.; Lecocq, A. New insight on the risk profile pertaining to lithium-ion batteries under thermal runaway as affected by system modularity and subsequent oxidation regime. *J. Energy Storage* **2022**, *52*, 104790. [CrossRef]
46. Willstrand, O.; Pushp, M.; Andersson, P.; Brandell, D. Impact of different Li-ion cell test conditions on thermal runaway characteristics and gas release measurements. *J. Energy Storage* **2023**, *68*, 107785. [CrossRef]
47. Koch, S.; Fill, A.; Birke, K.P. Comprehensive gas analysis on large scale automotive lithium-ion cells in thermal runaway. *J. Power Sources* **2018**, *398*, 106–112. [CrossRef]

ASME Journal of Electrochemical Energy Conversion and Storage
Online journal at:
https://asmedigitalcollection.asme.org/electrochemical

[redacted]
Electrochemical Safety Research Institutes,
UL Research Institutes,
5000 Gulf Fwy,
UHTB, Bldg 4, Rm 118,
Houston, TX 77204
e-mail: [redacted]

[redacted]
Electrochemical Safety Research Institutes,
UL Research Institutes,
5000 Gulf Fwy,
UHTB, Bldg 4, Rm 118,
Houston, TX 77204
e-mail: [redacted]

[redacted]
Electrified Powertrain Section,
Southwest Research Institute,
6220 Culebra Road,
San Antonio, TX 78238
e-mail: [redacted]

[redacted]
Electrified Powertrain Section,
Southwest Research Institute,
6220 Culebra Road,
San Antonio, TX 78238
e-mail: [redacted]

[redacted]
Electrochemical Safety Research Institutes,
UL Research Institutes,
5000 Gulf Fwy,
UHTB, Bldg 4, Rm 118,
Houston, TX 77204
e-mail: [redacted]

Characterization of Particulate Emissions From Thermal Runaway of Lithium-Ion Cells

Over the past decade, there has been a significant acceleration in the adoption of lithium-ion (Li-ion) batteries for various applications, ranging from portable electronics to automotive, defense, and aerospace applications. Lithium-ion batteries are the most used energy storage technologies due to their high energy densities and capacities. However, this battery technology is a potential safety hazard under off-nominal conditions, which may result in thermal runaway events. Such events can release toxic gaseous and particulate emissions, posing a severe risk to human health and the environment. Particulate emissions from the failure of two different cell chemistries—lithium iron phosphate (LFP) and nickel manganese cobalt oxide (NMC)—were studied. Experiments were conducted at multiple states of charge (SOC), and three repeats were performed at each SOC for each cell chemistry to examine the repeatability/variability of these events. Particulate emissions were characterized in terms of particulate matter mass (PM2.5), black carbon, and particle number (PN)/size. Failure of a single cell led to a significant release of particulate emissions, with peak emission levels being higher at the higher SOCs. A high level of variability was observed for a specific SOC for LFP cells, while NMCs exhibited relatively less variability. In general, much higher particulate emissions were observed for NMCs compared to LFPs at each SOC. For NMCs at 100% SOC, peak PN levels were ~$2.5 \times 10^{+09}$ particles/cc (part/cc), and black carbon levels were ~60 mg/m^3. For LFPs at 100% SOC, peak PN levels were ~$9.0 \times 10^{+08}$ part/cc, and black carbon levels were 2.5 mg/m^3.
[DOI: 10.1115/1.4065938]

Keywords: lithium-ion batteries, thermal runaway, particulate emissions, energy storage

1 Introduction

Lithium-ion (Li-ion) batteries have significantly impacted our modern world, serving as a vital source of power for a variety of portable electronic devices and electric vehicles, as well as contributing to renewable energy storage systems [1]. Nevertheless, the widespread use of Li-ion batteries has raised concerns about their safety, specifically the risk of thermal runaway events [2]. Thermal runaway can occur due to various off-nominal conditions, including electrical, mechanical, and thermal abuse [3]. Under these conditions, due to the increased internal temperature of Li-ion cells, a series of exothermic chemical reactions are triggered, leading to catastrophic failures, fires, and even explosions of the flammable gases released during this event [4].

Thermal runaway presents a critical safety concern due to the potential venting of gases and the ejection of particulate matter. Characterizing these safety risks is important for various stakeholders, including emergency responders, health researchers, government regulators, and other stakeholders responsible for developing standards and building solutions that advance human safety and sustainability. Research has shown that various gaseous species such as carbon dioxide, carbon monoxide, hydrogen, alkanes, alkenes, acid gases (such as hydrofluoric acid [HF]), and volatile organic compounds (VOCs) are produced during thermal runaway events [5–9]. These gaseous emissions introduce immediate risks, notably the potential for flammability and fire hazards. Accumulation of combustible gases in confined spaces can lead to explosive conditions, increasing the likelihood of fires or explosions. Additionally, VOC emissions can contribute to air pollution, which can have long-term environmental consequences. Some gases such as HF, formaldehyde, nitric oxide, and toluene [9] are highly toxic to human health, evident by their very low immediately dangerous to life and health levels.

[1]Corresponding author.
Manuscript received March 12, 2024; final manuscript received June 6, 2024; published online August 6, 2024. Assoc. Editor: Jun Xu.

While extensive research has been conducted in analyzing gases released during thermal runaway [10], investigation of particulate emissions during thermal runaway events is relatively less explored. Particulate matter emitted during thermal runaway can include materials like metals, metal oxides, carbonaceous soot, and organic chemicals. These emissions can transport toxic and hazardous materials, posing additional health and environmental risks [11]. Depending on their composition, morphology, concentration, and size distribution, these particles can have adverse health effects upon inhalation, contaminate soil and water sources, and impact ecosystems [12]. Moreover, these particles can include high-speed, high-temperature particles that can potentially ignite the flammable gases that are also released, further exacerbating the thermal runaway process [13]. Such particles could also influence and lead to other failure phenomena, such as high-voltage arc discharges, which could have serious consequences. Therefore, understanding and characterizing this ejecta are crucial for both comprehending the dynamics of thermal runaway and mitigating associated health, environmental, and fire risks. Multiple studies have observed the inherent variability of thermal runaway events [14,15]. It is to be noted that the variability in thermal runaway events can directly impact particulate emissions and release profiles during such occurrences.

A few recent studies have focused on characterizing particulate emissions during thermal runaway. The focus of all these studies has been on larger particulates (>2.5 μm in size). Zhang et al. [16] conducted an experiment to analyze gaseous and solid particle emissions during thermal runaway of a commercial 50 Ah, 3.65 V nickel manganese cobalt (NMC) cell. Gas chromatography and mass spectrometry (GC–MS) were used to determine the composition of the gases, while particle size analysis, ion chromatography, and inductively coupled plasma mass spectrometry were used for particle emission analysis. They detected 30 elements, most with a size less than 0.5 mm in diameter and a median size of approximately 397 μm. Chen et al. [17] utilized Fourier transform infrared, X-ray diffraction analysis, and GC–MS techniques to characterize the composition of ejected powder during the thermal runaway of an 18650 Li-ion cell. Their findings revealed that the ejected powder mainly consisted of carbon, metals, metal oxides, and organic chemicals. Additionally, the study reported particle size distributions ranging from 8.49 to 300.00 μm in ambient air and 5.94 to 210.04 μm in an Argon atmosphere. Barone et al. [18] utilized scanning electron microscopy (SEM) and energy-dispersive X-ray spectroscopy to investigate the morphology and elemental composition of particulates emitted during thermal runaway incidents in lithium iron phosphate (LFP), NMC, and lithium cobalt oxide batteries. Yang et al. [19] utilized SEM, X-ray fluorescence, and laser particle size analysis to examine the morphology, determine chemical composition, and analyze the particle size distribution of particles emitted during thermal runaway events in NMC cathodes. Furthermore, they investigated the biotoxicity of these particles and compared it to the pristine cathode material. Their study revealed an immediate inhibition of bacterial respiratory activities and observed cell membrane damage following a 5-h exposure to emitted particles. Wang et al. [13] conducted a study investigating particle emissions during the thermal runaway of Li-ion cells with various NMC cathodes. This study examined elemental composition, particle size distribution, morphology, and crystal structure. Their study concluded that most of the particles emitted were less than 0.85 mm and contained elements with potential health and environmental risks. In general, very few studies reported in the literature investigated emissions of smaller particles from battery fires. These particles tend to remain airborne for much longer durations, thereby posing a risk to human health and the environment. Premnath et al. [20] examined fine (less than 2.5 μm) particulate emissions during thermal runaway events in LFP and NMC modules. Their study encompassed measurements of particulate matter mass (PM2.5), real-time particle number and size, as well as real-time black carbon. Notably, their findings revealed emission rates that were 5–6 orders of magnitude higher than those observed in the exhaust of a contemporary heavy-duty diesel engine. This study also demonstrated that a significant release of particles falls well within the respirable size range.

This research program was formulated to address the critical knowledge gap that exists in the literature in understanding fine particulate emissions from battery fires. This program involved examining these emissions from cell-level failure events at different states of charge (SOC) varying from 100% to 10%. Experiments were conducted in triplicates to understand the variability/repeatability of these emissions. Thermal abuse was applied to the test articles in a controlled manner to initiate thermal runaway. Particulate emissions were characterized in detail using multiple state-of-the-art measurement techniques to gain information on black carbon, particle number, and particulate matter emissions. Cells from two different cathode chemistries were studied for pure scientific data gathering and not for comparison between the two chemistries. The results obtained are specific to the cell design, size, and chemistry studied.

2 Experimental Methods

2.1 Test Articles and Test Matrix. This paper focuses on two cell types composed of LFP and NMC cathode chemistries. The NMCs were pouch type, and the LFPs were prismatic metal can type. Both cells considered in this study were fresh cells. The NMC cells were harvested from a module used in an automotive electric vehicle, while the LFP cells were extracted from a battery module used for applications such as energy storage in recreational vehicles, vans, boats, and golf carts. Additional details about the two cell types are listed in Table 1.

The test matrix is shown in Table 2. Three repeats were conducted for each cell type at each SOC. External heating was used as the abuse mechanism, where the test article was heated at a rate of 10 °C/min until the maximum rated temperature of the heater pads was reached (220 °C). Once the peak temperature was achieved, the temperature was held at 220 °C until thermal runaway occurred. The objectives of the test matrix were to examine the repeatability/variability of particulate emissions during thermal runaway and to understand the impact of cell SOC on these emissions. No suppression systems were engaged at any point during these tests, and the thermal runaway event was allowed to unfold naturally.

The LFP cell was instrumented with five thermocouples and four heater pads at various locations, as shown in Fig. 1. One additional

Table 1 Specification of the test articles

Cell type	Specification
LFP cells	Nominal capacity: 50 Ah Nominal voltage: 3.2 V Weight: 1129 g
NMC cell	Nominal capacity: 71 Ah Nominal voltage: 3.7 V Weight: 985 g

Table 2 Test matrix

Cell chemistry	Repeats	State of charge (%)
LFP	1 pilot test	100
LFP	3	100
LFP	3	50
LFP	3	30
LFP	3	10
NMC	1 pilot test	100
NMC	3	100
NMC	3	50
NMC	3	30
NMC	3	10

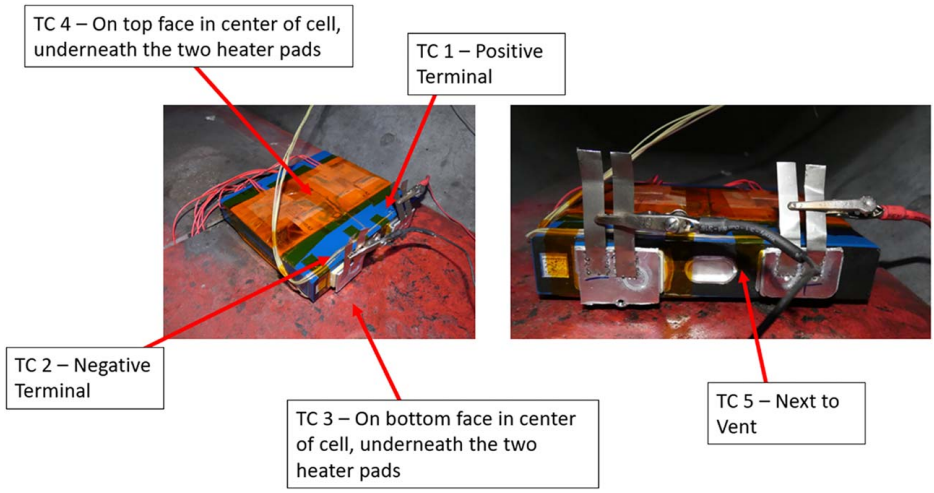

Fig. 1 LFP cell instrumentation and setup

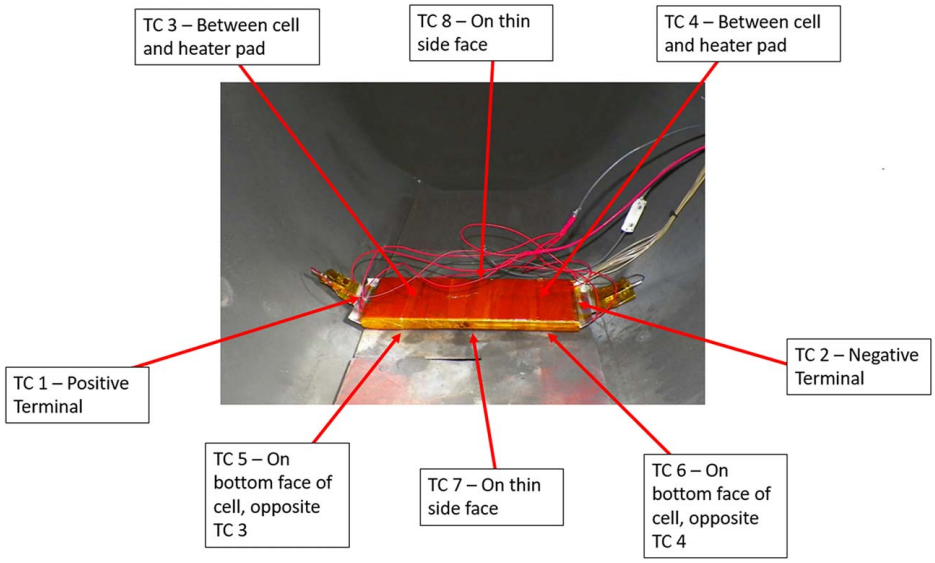

Fig. 2 NMC cell instrumentation and setup

Table 3 Cell conditioning protocol

Cell type	Charging protocol
LFP	Charge at 25 A until 3.6 V, then charge at 3.6 V until the current is less than 1 A Rest for 1 h Discharge at 25 A until 2.5 V Rest for 1 h Charge at 25 A until the desired SOC level based off discharge capacity calculated previously
NMC	Charge at 21.32 A until 4.2 V and then charge at 4.2 V until the current is less than 0.71 A Rest for 1 h Discharge at 35.5 A until 2.7 V Rest for 1 h Charge at 21.32 A until desired SOC level based off discharge capacity calculated previously

thermocouple was used to measure ambient temperature. The cell voltage was also monitored. Details for the NMC cell are shown in Fig. 2. The cell voltage was also monitored. Prior to each test, cells were charged to the test condition using the protocol shown in Table 3.

2.2 Test Chamber, Experimental Setup, and Emissions Analyzers. Testing was conducted in one of the test chambers at SwRI's Energy Storage Technology facility. The test chamber is equipped with a pollution abatement system that enables sampling of particulate and gaseous emissions from Li-ion battery fires. The

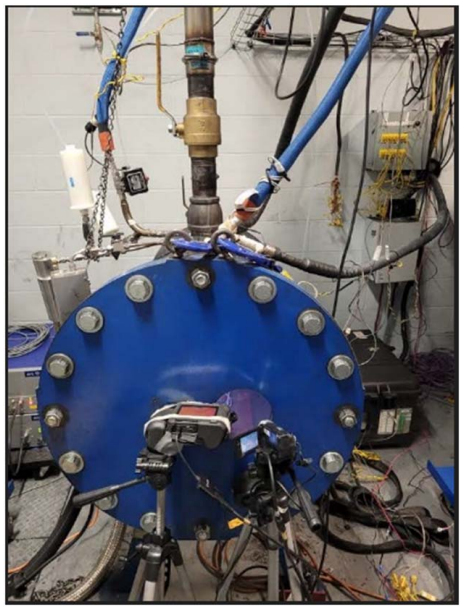

Fig. 3 Test chamber setup

test chamber and the exhaust piping from which particulate measurements were conducted are shown in Fig. 3. The chamber was sealed as much as possible to ensure that any effluents from the thermal runaway process passed through the exhaust piping at the top. Sample probes were installed in the pipe, and stainless-steel transfer lines were used to transport samples to the particulate analyzers. Good aerosol sampling practices were adopted to ensure minimal losses of particulates across the entire sample train from the probe to the instrument. Engineers and technicians controlled and observed the test outside the test cell to ensure personnel safety.

Figure 4 provides a schematic of the test setup. The particle instruments extracted samples from the pipe with a constant air/gas flowrate of ~34.8 lpm. Battery emissions were drawn into the exhaust pipe diluted by air from the ambient environment in the test cell. It is to be noted that sufficient oxygen was always available to sustain combustion.

Detailed characterization of particulate emissions was conducted using the methods described below. It is to be noted that the aerosol sampling techniques used during this program were primarily to measure particles sub-2.5 μm in size—referred to as fine particulates. Battery fires result in the release of larger particulates as well. However, measurement of these emissions was beyond the scope of this program. Characterization of larger particulates requires careful design of isokinetic sample probes and low-loss sampling systems.

2.2.1 Cambustion DMS500 Fast Particle Analyzer. The DMS500 is a real-time nanoparticle size spectrometer that simultaneously measures particle size distribution and number concentration [21]. The instrument can detect and measure particles from 5 nm to 1000 nm in size. The instrument operates on an electrical mobility (size to charge ratio) based classification scheme wherein it charges sample particles using a unipolar corona charger and, subsequently, classifies these particles using twenty-two electrometers based on their electrical mobility (a function of particle charge to size ratio). Signals from these electrometers are processed to generate spectral data on a real-time basis (1 Hz). The instrument also has a built-in dilution system that can be engaged to ensure that the electrometer channels do not get overwhelmed or saturated. For most of the campaign, a dilution setting of ~1500:1 was used.

2.2.2 AVL Micro-Soot Sensor. An AVL micro-soot sensor (MSS), which operates based on a photo-acoustic measurement scheme, was used to measure real-time black carbon concentration [22]. Sample particles are exposed to modulated laser light, which results in an increase in temperature of strongly absorbing black carbon particles. This, in turn, results in the heating of gas surrounding these particles, leading to the generation of sound waves that are detected by a sensitive microphone. This signal is proportional to the concentration of black carbon mass in the measurement chamber. The upper and lower limits of the MSS's detection capability are 50 mg/m^3 and 5 μg/m^3, respectively. The MSS includes an internal dilution system operated at a constant dilution ratio of 3:1.

2.2.3 Gravimetric Particulate Matter Mass Filter Measurement. A Sierra BG-3 partial flow sampling system was used to collect samples on TX40 media 47-mm diameter filters [23]. These filters were pre- and postweighed after sample collection to determine PM emission rate. The BG-3 includes a radial inflow porous stainless-steel dilution tunnel that helps dilute the sample with clean, particulate-free air with minimal losses. The ability to control sample dilution ensures that the filter loading

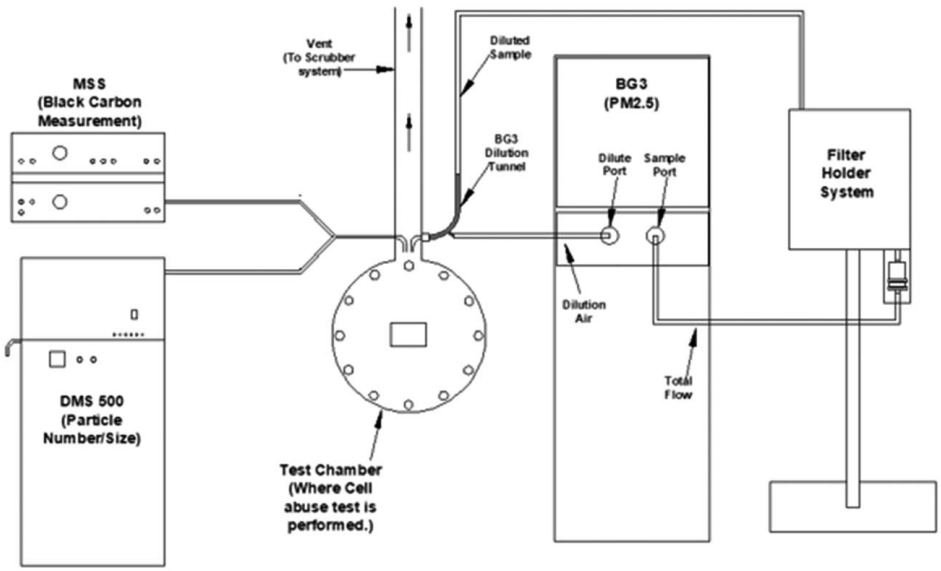

Fig. 4 Schematic of test chamber setup with particulate analyzers

Table 4 Summary of observations for the cell-level abuse test

Battery chemistry	SOC (%)	Round	Peak temperature (°C)	Fire?	Venting location	Pretest weight (g)	Posttest weight (g)
LFP	100	1	373	No	Vent between terminals	1131	920
LFP	100	2	293	No	Vent between terminals	1130	999
LFP	100	3	426	No	Vent between terminals	1127	919
LFP	50	1	271	No	Vent between terminals	1125	944
LFP	50	2	660	Yes	negative terminal	1126	941
LFP	50	3	303	No	back side, negative terminal side[a]	1130	946
LFP	30	1	244	No	back side, negative terminal side[a]	1130	957
LFP	30	2	242	No	Vent between terminals	1135	973
LFP	30	3	227	No	Vent between terminals	1133	997
LFP	10	1	230	No	Vent between terminals	1130	1014
LFP	10	2	231	No	Vent between terminals	1126	994
LFP	10	3	225	No	Vent between terminals	1127	1017
NMC	100	1	1300	Yes	Tabs	982	474
NMC	100	2	1300	Yes	Tabs	983	523
NMC	100	3	1300	Yes	Tabs	981	547
NMC	50	1	697	No	Tabs	980	783
NMC	50	2	754	No	Tabs	983	778
NMC	50	3	768	No	Tabs	981	788
NMC	30	1	576	No	Tabs	984	804
NMC	30	2	570	No	Tabs	982	805
NMC	30	3	561	No	Tabs	983	805
NMC	10	1	342	No	Tabs	982	833
NMC	10	2	384	No	Tabs	982	829
NMC	10	3	307	No	Tabs	981	839

[a]Initial venting accompanied by sparks.

remains within acceptable levels, which would otherwise lead to the filter overloading and tearing (thereby voiding the measurement).

3 Results and Discussion

Results that include physical observations, black carbon emissions, particle number emissions and size signatures, and PM2.5 emissions will be discussed for all cell-level tests conducted as a part of this project. Table 4 summarizes observations made relative to the test article, and Table 5 summarizes particulate emissions data for all tests.

3.1 Physical Observations. All tests were executed using a similar process. Figure 5 serves as an example and provides information on how a specific test was executed from start to finish. Turning on the power to the heater was referred to as the start of the test. It took ~20 min from the start of the test until a peak temperature of 220 °C was reached (also the upper threshold temperature of the heater pads used). Instruments for detecting particulates were placed on stand-by mode once this temperature was reached. This mode prepared the instruments for sampling and led to ambient air being drawn over the test article, thereby resulting in a minor decrease in temperature, as highlighted in the figure. The instruments were placed on "sample mode" once thermal runaway occurred, confirmed visually by venting and by a rapid increase in test article temperatures. The power to the heater pads was turned off during the onset of thermal runaway. Particulate measurements were collected either until the instruments were saturated or until concentrations returned to ambient levels. Following which, a blower system was engaged to evacuate the test chamber and exhaust emissions outside the building after flowing through a filtration/scrubbing system. Engagement of the scrubbing system resulted in a large draw of ambient laboratory air over the test article, thereby cooling it further. The test article was monitored in the test chamber to cool down to temperatures below 50 °C for at least an hour prior to conducting postmortem analysis.

Tables 4 and 5 summarize the results of all the tests conducted in this program. For the LFP chemistry, peak temperatures were highest for 100% SOC, and then steadily decreased as SOC decreased. At 100% SOC, the average peak temperature was 364 °C, and it decreased to an average of 229 °C at 10% SOC. During one of the 50% SOC tests for the LFP chemistry, a fire was observed during thermal runaway, causing a spike in temperature resulting in a peak temperature of ~660 °C (round 2, 50% SOC, LFP test). For most of the LFP testing, venting occurred through the designated vent in the cell. However, for a few tests with 50% and 30% SOC, venting also occurred through the negative terminal, or the back side of the cell, opposite the terminals. Although peak temperatures observed for the NMC cells were much higher, fire was only observed during the 100% SOC tests. At 100% SOC, the thermocouples were destroyed in the fire for the NMC cells, therefore showing temperatures peaking out at the thermocouple limit. As the SOC decreased to 50%, 30%, and 10%, the average peak temperatures decreased to 740 °C, 569 °C, and 344 °C, respectively. For all NMC tests, venting occurred through the seals near the tabs on the cells.

3.2 Black Carbon Emissions. Thermal runaway of both cell chemistries resulted in black carbon emissions. There could be multiple sources for black carbon generation from a Li-ion cell. Graphite, which is a stable form of carbon, is commonly used as the anode active material in Li-ion cells. Carbon additives may also be used in electrodes to enhance electrical conductivity. For events accompanied by combustion and fire, these measurements may also include the emission from combustion. Detailed material characterization of the test articles was beyond the scope of this article and will be included as a part of a future publication. Figure 6 provides real-time black carbon emissions profiles for LFP and NMC tests at various SOCs. Data from one of the repeats at each SOC have been presented in this figure to serve as an example of the release profile after the onset of thermal runaway. Typically, NMC tests resulted in higher black carbon levels than LFP tests. For most tests, peak emission levels were observed close to the onset of thermal runaway. Subsequently, additional excursions in black carbon levels were observed depending on how the event unfolded. For instance, the 100% NMC test yielded a peak close to 40 mg/m^3 early on, and a secondary release after about 75 s with a peak of ~4 mg/m^3. In the case of the 30% LFP test, black carbon activity was observed for ~300 s from the onset of thermal runaway. Environmental

Table 5 Summary of particulate emissions

Battery chemistry	SOC (%)	Round	PM2.5 emissions (g/h)	Black carbon emissions (mg/h)	Particle number emissions (part/h)
LFP	100	Pilot	1.75	0.47	$1.43 \times 10^{+14}$
LFP	100	1	1.78	0.18	$1.63 \times 10^{+14}$
LFP	100	2	1.24	0.02	$1.80 \times 10^{+13}$
LFP	100	3	2.58	0.52	$2.22 \times 10^{+14}$
LFP	50	1	0.28	0.00	$9.71 \times 10^{+12}$
LFP	50	2	1.38	0.17	$9.41 \times 10^{+13}$
LFP	50	3	0.52	0.04	$4.96 \times 10^{+13}$
LFP	30	1	0.94	0.18	$8.96 \times 10^{+13}$
LFP	30	2	0.03	0.00	$5.74 \times 10^{+11}$
LFP	30	3	0.06	0.00	$1.07 \times 10^{+10}$
LFP	10	1	0.05	0.00	$2.03 \times 10^{+10}$
LFP	10	2	0.18	0.00	$4.52 \times 10^{+12}$
LFP	10	3	0.01	0.00	$4.83 \times 10^{+11}$
NMC	100	Pilot	6.73	4.70	$2.89 \times 10^{+14}$
NMC	100	1	3.23	4.15	$1.15 \times 10^{+14}$
NMC	100	2	3.91	4.36	$1.21 \times 10^{+14}$
NMC	100	3	6.49	7.61	$1.25 \times 10^{+14}$
NMC	50	1	2.84	1.35	$1.93 \times 10^{+14}$
NMC	50	2	3.70	1.20	$1.61 \times 10^{+14}$
NMC	50	3	4.05	4.08	$1.73 \times 10^{+14}$
NMC	30	1	3.66	0.28	$5.32 \times 10^{+13}$
NMC	30	2	1.12	0.03	$9.11 \times 10^{+12}$
NMC	30	3	1.26	2.44	$9.31 \times 10^{+13}$
NMC	10	1	0.13	0.00	$4.52 \times 10^{+12}$
NMC	10	2	0.01	0.00	$0.00 \times 10^{+00}$[a]
NMC	10	3	0.01	0.00	$0.00 \times 10^{+00}$[a]

[a]Measured PN concentrations were similar to ambient background levels.

Protection Agency (EPA) guidelines suggest that PM concentrations at or below 12 $\mu g/m^3$ to be safe over a 24-hr exposure window. Levels above 500 $\mu g/m^3$ or 0.5 mg/m^3 are considered to be hazardous to human health. Black carbon is a key component of PM, and peaks of the order of 60 mg/m^3 were observed during some tests.

Figure 7 summarizes observations made for both cell chemistries in terms of average black carbon emissions and peak black carbon emissions observed for all tests conducted. Average emissions have been reported for the first 200 seconds following the onset of a thermal runaway, as the significant release of emissions occurred during this window. LFP tests conducted at a specific SOC exhibited considerable variability, making it difficult to extract a black carbon release trend as a function of SOC. It is to be noted that the variability was intrinsic to the test article, and the abuse test protocol applied for each test was the same. In the case of NMC tests, nominally, higher SOC resulted in higher peak emissions and higher average black carbon emissions. 10% SOC tests did not yield any black carbon emissions for both cell chemistries as the cells did not experience violent venting or thermal runaway. Some of the 30% SOC tests yielded black carbon emissions for both chemistries. In fact, one of the repeats at 30% SOC for the NMC chemistry resulted in a peak close to 7 mg/m^3, which is a significant amount of black carbon emissions.

3.3 Particulate Number Emissions. Particulate number emissions were measured using the DMS500 Fast Particle Sizer. This analytical technique detects all particulate phase emissions ranging from 5 nm to 1000 nm, and simultaneously provides number concentration and size distribution. Figure 8 provides real-time emissions for LFP and NMC tests conducted at different SOCs. High levels of particulate number emissions were observed for both chemistries. Peak levels observed with NMC tests were higher than those of LFP tests conducted at the corresponding SOC. Ambient PN levels in a laboratory setting or inside a house in the US are usually between 2000 and 4000 particles/cc (part/cc). Peak levels observed during the NMC tests were of the order of $2 \times 10^{+9}$ part/cc, which is 6 orders of magnitude higher than ambient levels. LFP tests yielded peak concentrations close to $8 \times 10^{+8}$ part/cc, which is also close to 6 orders of magnitude higher than ambient levels. Typically, the initial release during the onset of thermal runaway resulted in peak PN release levels. During some tests, high PN levels were observed even after the

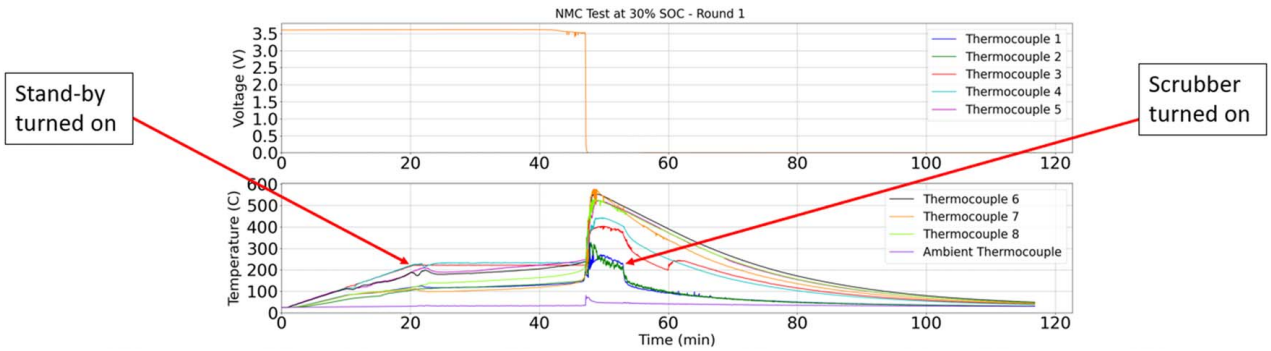

Fig. 5 Example plot outlining test sequence

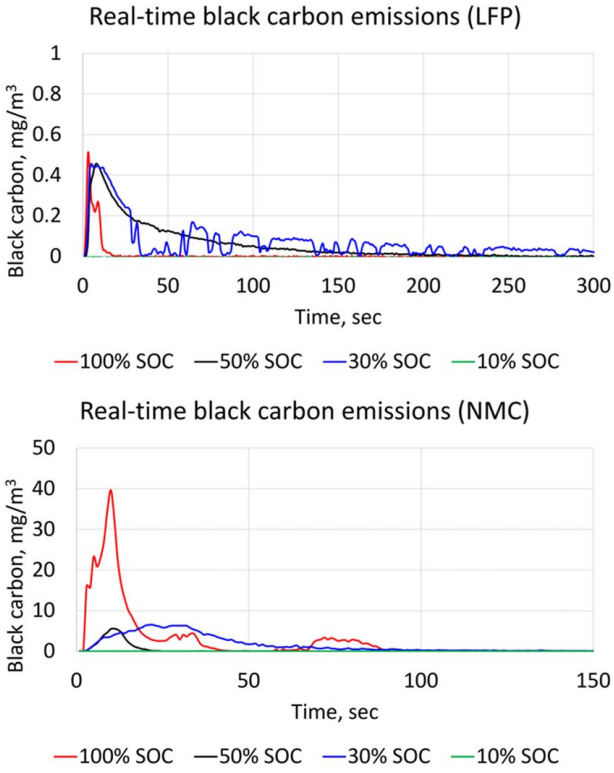

Fig. 6 Real-time profile of black carbon emissions

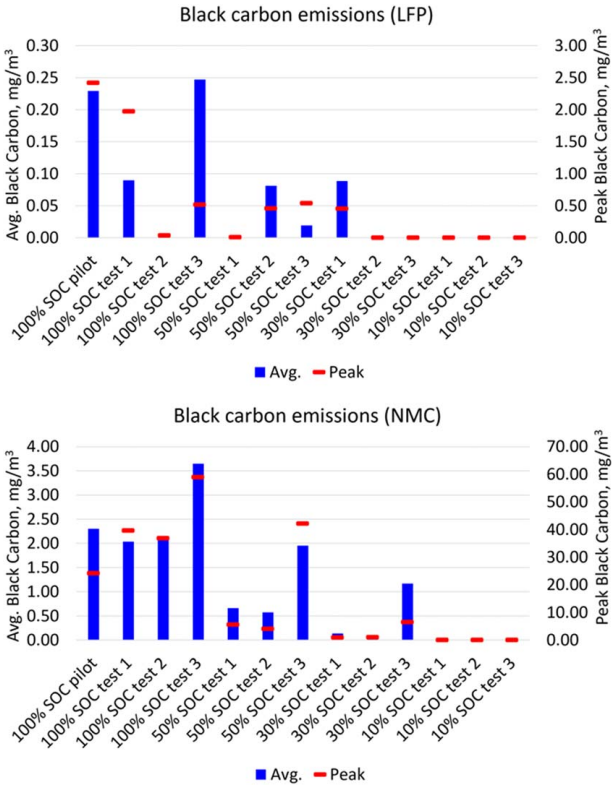

Fig. 7 Average and peak black carbon emissions for all tests

initial release event. It is to be noted that these high PN emissions were from the thermal runaway of a single cell. In real-world applications involving modules and packs composed of multiple cells, these emissions could scale dramatically if propagation of thermal runaway and failure occurs.

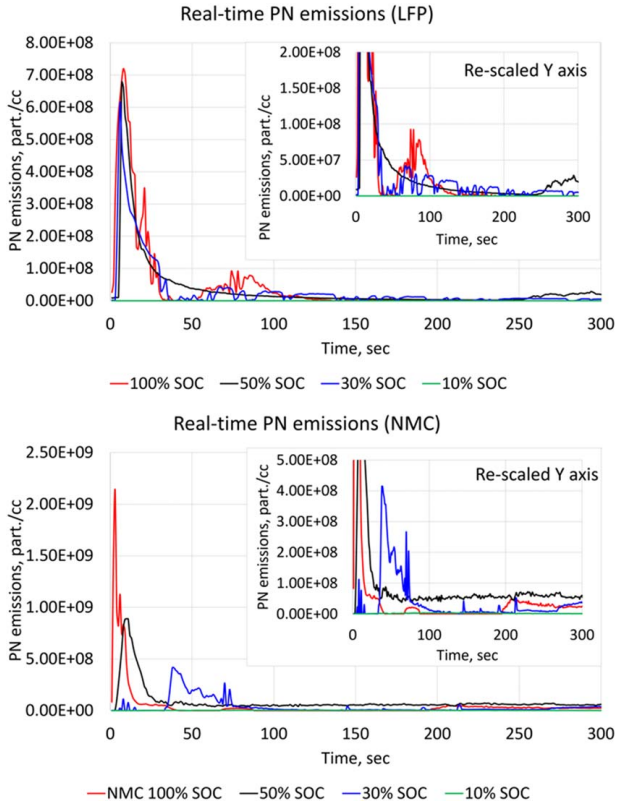

Fig. 8 Real-time profile of particle number emissions

Figure 9 summarizes information for all tests conducted for each cell chemistry at various SOCs. Similar to black carbon analysis, the average concentration observed over the first 200 s from the onset of thermal runaway has been presented. As observed with black carbon emissions, LFP tests exhibited variability in PN emissions as well at specific SOCs. Interestingly, peak PN levels observed during some of the 100%, 50%, and 30% SOC tests were in a similar range of $\sim 8 \times 10^{+8}$ part/cc. No significant PN emissions were observed during the 10% SOC tests. NMC tests resulted in higher PN emissions than LFP tests. In general, peak PN levels decreased with the decrease in SOC, although there were a couple of outliers. While no significant black carbon emissions were observed at 30% SOC for NMCs, significant PN emissions were observed at this SOC. Further, average PN emissions observed during the first 200 s following the onset of thermal runaway were higher for the 50% SOC tests compared to the 100% SOC tests. This was largely due to the release profiles, as shown in Fig. 9. The 100% NMC tests resulted in a very high PN level during the initial release immediately after the onset of thermal runaway, after which PN returned to lower levels. In the case of 50% NMC tests, PN levels remained high even after the initial peak event, as shown in Fig. 8.

3.4 Particulate Matter Mass Emissions. Thermal runaway results in the release of particulate matter composed of various species, including carbonaceous soot, metals, carbonates, and various hydrocarbons, among others. The experimental technique used to characterize PM2.5 emissions from cell abuse involved sampling all ejected constituents on borosilicate glass fiber filters. These filters have very high collection efficiencies and serve as a sensitive technique to better understand thermal runaway emissions. Unlike the other two measurements described in the previous sections, this technique does not generate real-time information. Instead, this batch sampling method was used to determine PM2.5 emissions throughout the entire event. For this program, sample collection on the filter media was performed using a

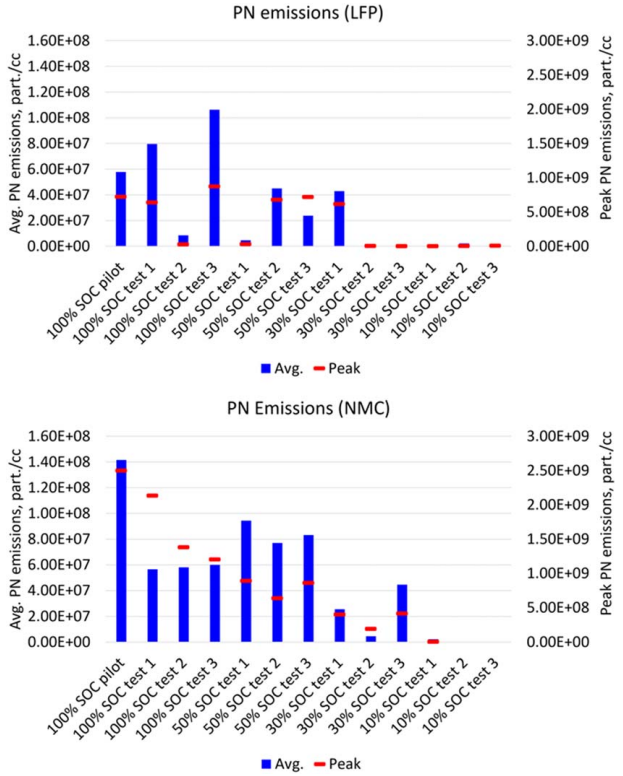

Fig. 9 Average and peak particle number emissions for all tests

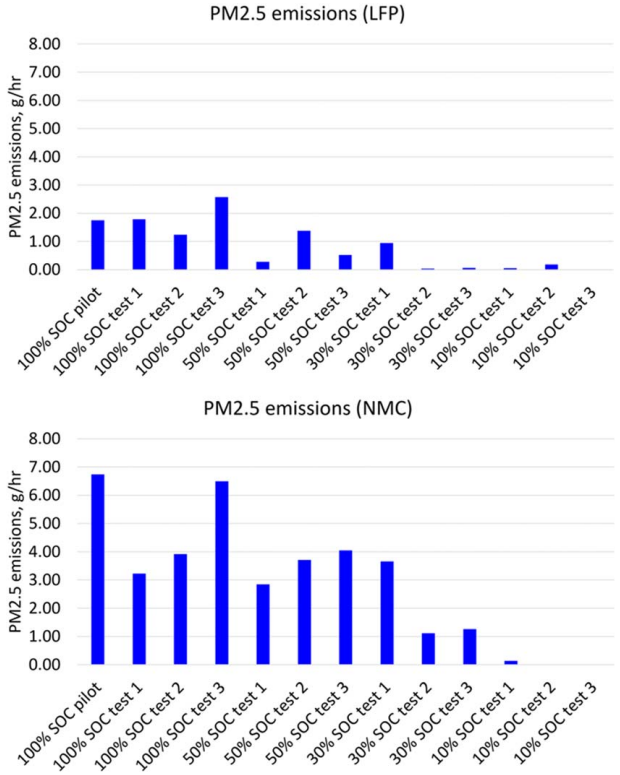

Fig. 10 PM2.5 emissions for all tests

Sierra BG-3 system. Sampling was started during the onset of thermal runaway and stopped either when the pressure drop across the filter reached 34 kPa (the upper threshold beyond which the sample filter will fail) or when PN concentration reported by the DMS500 reached ambient levels.

Figure 10 summarizes the PM2.5 emission rate for all tests conducted. PM2.5 emissions observed during NMC cell failures were higher than those observed with LFP tests. As observed with black carbon and PN emissions, LFP tests conducted at the same SOC exhibited variability in PM2.5 emissions. For both cell chemistries, 100% SOC resulted in higher PM2.5 emissions on an average basis, followed by 50%, 30%, and 10% SOCs. This trend suggests that higher SOC results in a more dramatic failure event with more ejecta release, which has been observed by other researchers. Additional research needs to be conducted to determine the composition and morphology of PM2.5 collected on the filters, which is beyond the scope of this program.

3.5 Size Signatures of Particulate Emissions. Size distributions of thermal runaway emissions were characterized using the DMS500 Fast Particle Analyzer. Figure 11 provides size signatures for both cell chemistries at various SOCs tested. Figure 12 summarizes the geometric mean number diameters of the size signatures for all tests conducted. One significant conclusion that can be drawn is the fact that the particulates emitted from cell failure were well within the human respirable size range. Further, high levels of emissions were also observed in the ultrafine particulate size range. These are defined as sub-100-nm particles and are known to be more toxic to human health as they tend to penetrate deeper into the human respiratory system and eventually diffuse into the bloodstream and reach various organs. In addition to the physical characteristics of these particulates, the chemical composition plays a critical role in terms of their impact on human health. For instance, cobalt is known to be poisonous, and its ingestion could lead to cardiomyopathy and a host of other health conditions that include nerve, vision, hearing, and thyroid problems [24]. Likewise, inhalation of nickel could lead to respiratory and neurological illnesses, in addition to nickel being a known carcinogen [25]. Figure 12 suggests that higher test-to-test variability in GNMD was observed during LFP tests at a given SOC compared to NMC tests. Also, NMC tests resulted in particle size signatures

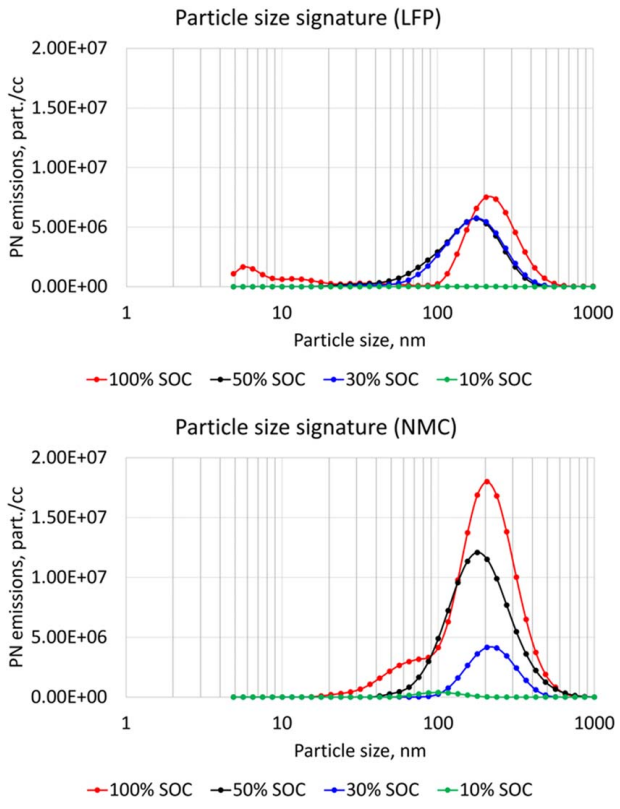

Fig. 11 Size signature of particulate emissions for all tests

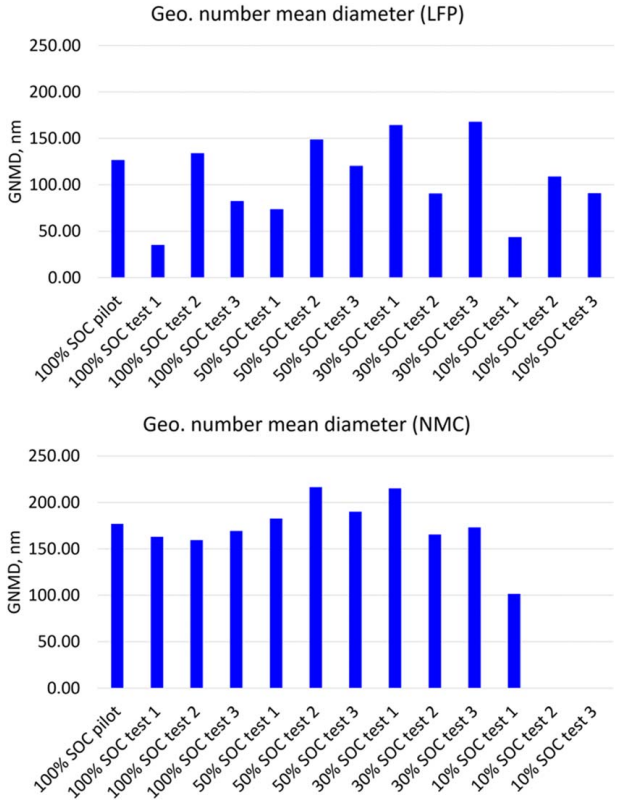

Fig. 12 Geometric number mean diameter analysis of size signatures for all tests

with larger size modes. Interestingly, for both cell chemistries, a decrease in SOC did not dramatically change the size signature, but instead, resulted in changes in peak levels.

4 Conclusions

The focus of this program was to conduct a detailed investigation of particulate emissions from Li-ion cell failure. Two commonly used Li-ion cell chemistries, LFP and NMC, were included as a part of this program. The LFP cells were prismatic metal can cells, while the NMCs were prismatic pouch cells. Cells were induced into thermal runaway using heating as the abuse method for all tests conducted. The test matrix was designed to gain knowledge of the impact of cell chemistry and SOC on thermal runaway particulate emissions and to understand the repeatability/variability associated with cell failure events. For each cell type, three repeats of overheat failure tests were conducted at 100%, 50%, 30%, and 10% SOCs. All tests were conducted in a blast chamber equipped with an exhaust pipe from which particulate emissions were sampled from inception to completion of the thermal runaway process. Real-time black carbon emissions, PN, and size distribution were measured, along with PM2.5, using state-of-the-art instrumentation. Results suggest the following:

- Thermal runaway of the cells tested as part of this program resulted in a significant release of particulate emissions. Peak PN concentrations of the order of $1 \times 10^{+09}$ were 6 orders of magnitude higher than typical ambient PN concentrations. Likewise, peak black carbon levels (~40 mg/m^3 observed during some tests) were also much higher than safe human exposure limits.
- Cell form factor, design, chemistry, composition of electrodes and electrolytes, and capacity could influence emission levels. At 100% SOC, NMC tests yielded average black carbon levels of ~2.2 mg/m^3, PN levels of $\sim 6 \times 10^{+07}$ part/cc, and PM2.5 emissions of ~5.1 g/h. For tests conducted with LFP cells at 100% SOC, average black carbon levels ranging from 0.1 to 0.25 mg/m^3, PN levels of $\sim 8 \times 10^{+07}$ part/cc, and PM2.5 emissions of ~1.6 g/h were observed.
- Results from three identical cell abuse tests at each SOC suggest that there can be significant variability in emissions. This observation is valid for both cell chemistries, with LFP cells exhibiting more variability than NMC cells.
- Among NMC tests, higher SOC tests resulted in higher peak PN concentrations. These concentrations were of the order of $1 \times 10^{+09}$ to $2 \times 10^{+09}$ part/cc. PM2.5 emissions also showed an increase with an increase in SOC. In the case of LFP tests, peak PN concentrations were reasonably similar for 100% and 50% tests (of the order of $7 \times 10^{+08}$ part/cc). However, average PN concentrations and PM2.5 decreased with a decrease in SOC.
- Size signatures of the thermal runaway process indicated emissions well within the respirable size range. Further, a large fraction of these particulates was in the ultrafine size range (<100 nm), which is known to have a more adverse impact on human health.

Knowledge of particulate emissions from battery fires is essential to assess the impact such an event would have on personnel in the vicinity, first responders (and their protective gear), operators, and the environment. Such information is also critical to better understand failure modes such as high-voltage arcing and thermal runaway propagation and to develop mitigation strategies. This program serves to address a critical knowledge gap in understanding some aspects of particulate emissions from cell abuse at various states of charge for cells of two different cathode chemistries and capacities. Future research should examine other cell chemistries, formats, abuse mechanisms, and module and pack-level test articles. Further, additional details about particulate emissions, such as composition and morphology, should be examined.

Acknowledgment

This work was supported by Underwriters Laboratories Research Institutes. The authors acknowledge Dr. Imad Khalek (Institute Engineer) for his review and comments on the manuscript. The authors also acknowledge the following SwRI staff members for their contribution in making this program successful—Mr. Mickey Argo (Assistant Manager), Mr. Daniel Preece (Supervisor), Mr. Angel Herrera (Technician), Mr. Taylor Mraz (Technician), Mr. Isaiah Hernandez (Technician), and Mr. Mario Guillen (Staff Technician).

Funding Data

- UL Research Institutes.

Conflict of Interest

There are no conflicts of interest.

Data Availability Statement

The datasets generated and supporting the findings of this article are obtainable from the corresponding author upon reasonable request.

References

[1] Jeevarajan, J. A., Joshi, T., Parhizi, M., Rauhala, T., and Juarez-Robles, D., 2022, "Battery Hazards for Large Energy Storage Systems," ACS Energy Lett., **7**(8), pp. 2725–2733.
[2] Velumani, D., and Bansal, A., 2022, "Thermal Behavior of Lithium-and Sodium-Ion Batteries: A Review on Heat Generation, Battery Degradation, Thermal Runway—Perspective and Future Directions," Energy Fuels, **36**(23), pp. 14000–14029.

[3] Essl, C., Golubkov, A. W., and Fuchs, A., 2020, "Comparing Different Thermal Runaway Triggers for Two Automotive Lithium-Ion Battery Cell Types," J. Electrochem. Soc., **167**(13), p. 130542.
[4] Wang, Q., Mao, B., Stoliarov, S. I., and Sun, J., 2019, "A Review of Lithium Ion Battery Failure Mechanisms and Fire Prevention Strategies," Prog. Energy Combust. Sci., **73**(Special issue Fire Safety), pp. 95–131.
[5] Golubkov, A. W., Fuchs, D., Wagner, J., Wiltsche, H., Stangl, C., Fauler, G., Voitic, G., Thaler, A., and Hacker, V., 2014, "Thermal-Runaway Experiments on Consumer Li-Ion Batteries With Metal-Oxide and Olivin-Type Cathodes," RSC Adv., **4**(7), pp. 3633–3642.
[6] Larsson, F., Andersson, P., Blomqvist, P., Lorén, A., and Mellander, B. E., 2014, "Characteristics of Lithium-Ion Batteries During Fire Tests," J. Power Sources, **271**, pp. 414–420.
[7] Larsson, F., and Mellander, B. E., 2014, "Abuse by External Heating, Overcharge and Short Circuiting of Commercial Lithium-Ion Battery Cells," J. Electrochem. Soc., **161**(10), pp. A1611–A1617.
[8] Larsson, F., Andersson, P., and Mellander, B. E., 2016, "Lithium-Ion Battery Aspects on Fires in Electrified Vehicles on the Basis of Experimental Abuse Tests," Batteries, **2**(2), p. 9.
[9] Nedjalkov, A., Meyer, J., Köhring, M., Doering, A., Angelmahr, M., Dahle, S., Sander, A., Fischer, A., and Schade, W., 2016, "Toxic Gas Emissions From Damaged Lithium Ion Batteries—Analysis and Safety Enhancement Solution," Batteries, **2**(1), p. 5.
[10] Qiu, M., Liu, J., Cong, B., and Cui, Y., 2023, "Research Progress in Thermal Runaway Vent Gas Characteristics of Li-Ion Battery," Batteries, **9**(8), p. 411.
[11] Sun, J., Li, J., Zhou, T., Yang, K., Wei, S., Tang, N., Dang, N., Li, H., Qiu, X., and Chen, L., 2016, "Toxicity, a Serious Concern of Thermal Runaway From Commercial Li-Ion Battery," Nano Energy, **27**, pp. 313–319.
[12] Quant, M., Willstrand, O., Mallin, T., and Hynynen, J., 2023, "Ecotoxicity Evaluation of Fire-Extinguishing Water From Large-Scale Battery and Battery Electric Vehicle Fire Tests," Environ. Sci. Technol., **57**(12), pp. 4821–4830.
[13] Wang, H., Wang, Q., Jin, C., Xu, C., Zhao, Y., Li, Y., Zhong, C., and Feng, X., 2023, "Detailed Characterization of Particle Emissions Due to Thermal Failure of Batteries With Different Cathodes," J. Hazard. Mater., **458**, p. 131646.
[14] Zhang, L., Yang, S., Liu, L., and Zhao, P., 2022, "Cell-to-Cell Variability in Li-Ion Battery Thermal Runaway: Experimental Testing, Statistical Analysis, and Kinetic Modeling," J. Energy Storage, **56**, p. 106024.
[15] Walker, W. Q., Darst, J. J., Finegan, D. P., Bayles, G. A., Johnson, K. L., Darcy, E. C., and Rickman, S. L., 2019, "Decoupling of Heat Generated From Ejected and Non-Ejected Contents of 18650-Format Lithium-Ion Cells Using Statistical Methods," J. Power Sources, **415**, pp. 207–218.
[16] Zhang, Y., Wang, H., Li, W., and Li, C., 2019, "Quantitative Identification of Emissions From Abused Prismatic Ni-Rich Lithium-Ion Batteries," ETransportation, **2**, p. 100031.
[17] Chen, S., Wang, Z., and Yan, W., 2020, "Identification and Characteristic Analysis of Powder Ejected From a Lithium Ion Battery During Thermal Runaway at Elevated Temperatures," J. Hazard. Mater., **400**, p. 123169.
[18] Barone, T. L., Dubaniewicz, T. H., Friend, S. A., Zlochower, I. A., Bugarski, A. D., and Rayyan, N. S., 2021, "Lithium-Ion Battery Explosion Aerosols: Morphology and Elemental Composition," Aerosol Sci. Technol., **55**(10), pp. 1183–1201.
[19] Yang, Y., Fang, D., Maleki, A., Kohzadi, S., Liu, Y., Chen, Y., Liu, R., Gao, G., and Zhi, J., 2021, "Characterization of Thermal-Runaway Particles From Lithium Nickel Manganese Cobalt Oxide Batteries and Their Biotoxicity Analysis," ACS Appl. Energy Mater., **4**(10), pp. 10713–10720.
[20] Premnath, V., Wang, Y., Wright, N., Khalek, I., and Uribe, S., 2022, "Detailed Characterization of Particle Emissions From Battery Fires," Aerosol Sci. Technol., **56**(4), pp. 337–354.
[21] Reavell, K., Hands, T., and Collings, N., 2002, "A Fast Response Particulate Spectrometer for Combustion Aerosols," SAE Trans., pp. 1338–1344.
[22] Schindler, W., Haisch, C., Beck, H. A., Niessner, R., Jacob, E., and Rothe, D., 2004, "A Photoacoustic Sensor System for Time Resolved Quantification of Diesel Soot Emissions," SAE Trans., pp. 483–490.
[23] Fanick, E. R., and Premnath, V., 2020, "Comparison of Partial and Total Dilution Systems for the Measurement of Polycyclic Aromatic Hydrocarbons and Hydrocarbon Speciation in Diesel Exhaust," SAE Technical Paper 2020-01-2190, p. 8.
[24] Wahlqvist, F., Bryngelsson, I. L., Westberg, H., Vihlborg, P., and Andersson, L., 2020, "Dermal and Inhalable Cobalt Exposure—Uptake of Cobalt for Workers at Swedish Hard Metal Plants," PLoS One, **15**(8), p. e0237100.
[25] Genchi, G., Carocci, A., Lauria, G., Sinicropi, M. S., and Catalano, A., 2020, "Nickel: Human Health and Environmental Toxicology," Int. J. Environ. Res. Public Health, **17**(3), p. 679.

scientific reports

Check for updates

OPEN

Coastal wetland deposition of cathode metals from the world's largest lithium-ion battery fire

[redacted]

Fires at lithium-ion battery storage facilities pose emerging environmental risks that remain largely undocumented under real-world conditions. Following a major fire at the world's largest Battery Energy Storage System (BESS) in Moss Landing, California, we conducted rapid, high-resolution soil surveys to quantify metal fallout in adjacent estuarine wetlands. Field-portable X-ray fluorescence (FpXRF), validated by SEM/EDS, laboratory XRF, and ICP-MS, revealed a significant but transient surface enrichment of nickel (Ni), manganese (Mn), and cobalt (Co). This enrichment had Ni: Co mass ratios near 2:1 serving as a geochemical fingerprint of NMC-type cathode materials. The metals were confined to a shallow surface layer (< 5 mm). Surface concentrations declined rapidly following precipitation and tidal inundation. The fallout's thin, transient and patchy distribution would have eluded standard coring methods but was detected through spatially intensive FpXRF sampling, highlighting the importance of rapid detection and the mobilization of metals into wetland ecosystems. These findings underscore the need for adaptive environmental monitoring following battery fires and raise critical considerations for ecosystem protection and infrastructure as energy storage systems expand.

Rapid growth of distributed energy storage systems in recent years reflects the global need to store power from renewable energy sources and to regulate electrical systems[1–3]. Lithium-ion batteries (LIBs) are the most widely used type of electrochemical energy storage, as they offer high energy and power density compared to other battery technologies[4]. However, electrochemical energy storage and the use and disposal of LIBs involves inherent risks, such as thermal runaway[5] which can lead to the release of potentially toxic compounds from battery materials[6], and localized deposition of battery-associated metals in adjacent ecosystems[7], with, potentially, long-term implications for terrestrial, aquatic, and human health.

Establishing robust environmental baselines in areas surrounding energy storage systems and achieving adequate spatial and temporal coverage to identify contamination after emergency release are both logistically difficult and often cost-prohibitive. In this context, portable and cost-effective technology such as X-ray fluorescence (FpXRF) offers a means of collecting high-density data, serving as a valuable complement to traditional laboratory-based analytical methods.

On 16 January 2025, a large fire engulfed the largest lithium-ion battery (LIB) Battery Energy Storage System (BESS) in the world, burning actively for at least 2 days. This was followed by a smaller reignition on 18 February 2025. Owned by Vistra Corporation, the BESS is in Moss Landing, California, immediately adjacent to Elkhorn Slough, a Ramsar site recognized as a wetland of international importance[8]. The fire affected the core of the facility (Phase 1) which had a capacity of 300 MW/1200 megawatt-hours (MWh) and was equipped with LG Energy Solution's TR1300 battery rack systems[9]. The fire destroyed approximately 75% of the facility[10] and produced a smoke plume visible from tens of kilometers away, depositing ash and soot across the surrounding area (Fig. 1a). Due to potential toxicity, including possible exposure to hydrogen fluoride, evacuation orders and road closures were issued. Residents were permitted to return 2 days after the fire began[11].

Controlled experiments show Li-ion battery fires emit metal-bearing aerosols (notably Ni–Co–Mn) and other toxicants, which can deposit downwind[6]. Three days after the fire, we rapidly mobilized to assess whether surface soils at Hester Marsh, a wetland restoration area within the Elkhorn Slough National Estuarine Research Reserve (ESNERR), only a few km from the Moss Landing facility had been affected by the fallout material from the smoke plume. Coincidentally, we had collected baseline surface soil elemental data in the same area for other research purposes with an FpXRF in 2023 (Fig. 2).

[1]Moss Landing Marine Laboratories, San Jose State University, 8272 Moss Landing Rd., Moss Landing, CA 95039, USA. [2]Elkhorn Slough National Estuarine Research Reserve, 1700 Elkhorn Road, 95076 Royal Oaks, CA, USA. ✉email: [redacted]@sjsu.edu

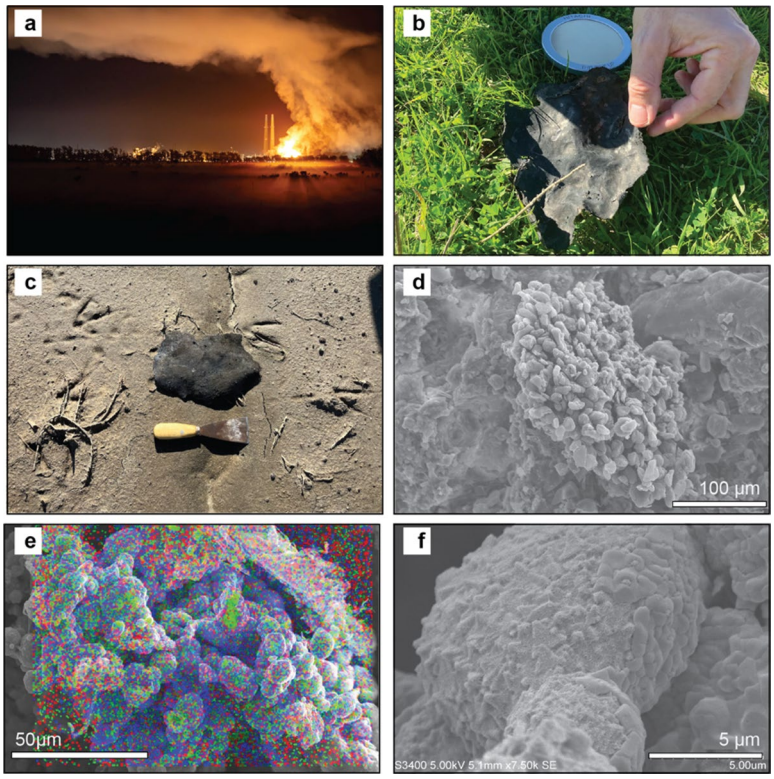

Fig. 1. (**a**) Photo of the battery fire and the smoke plume on January 16th, 2025. The picture is looking south towards the smokestacks of the old Moss Landing power plant and shows the smoke plume hovering Elkhorn Slough and Hester marsh to the east (Photo credit: Mike Takaki). (**b**–**c**) Field photographs showing burned battery fragments from the Vistra battery facility fire collected near transect T12 (B) and transect T8 (C). (**d**) Scanning electron microscope (SEM) images of cathode material aggregate composed of multiple Nickel Manganese Cobalt (NMC) microparticles; (**e**) Energy-dispersive X-ray spectroscopy (EDS) elemental map highlighting the spatial distribution of nickel (Ni, red), manganese (Mn, blue), and cobalt (Co, green). (**f**) A SEM close-up of a single NMC particle.

The Moss Landing battery facility is located within a complex and vulnerable landscape. It sits adjacent to Elkhorn Slough, one of California's largest estuaries, near the town of Moss Landing, and is surrounded by intensively farmed agricultural land. The fallout from the fire's smoke plume raises serious concerns about contamination of soils, water, and vegetation in this region.

Here, we report on the extent and dynamics of cathode metal contamination in estuarine soils immediately following the world's largest lithium-ion battery fire. By combining rapid, high-resolution field surveys with laboratory validation, we tracked the deposition and short-term fate of battery-derived metals in a sensitive wetland ecosystem. Our findings provide rare real-world evidence of the environmental footprint of large-scale battery fires, underscore the value of having a baseline near industrial sites that pose contamination risks, and demonstrate the utility of FpXRF as a practical tool for rapid and spatially intensive environmental monitoring.

Specifically, we test whether the Moss Landing fire deposited a thin surface veneer of battery-associated metals in adjacent wetlands that differ relative to 2023 baseline conditions and whether composition is consistent with NMC cathode material, using a high-density FpXRF survey validated with SEM/EDS, LpXRF, and ICP-MS.

Study area and methodology

Elkhorn Slough is a tide-dominated estuary that in the past 150 years has lost significant vegetated marsh area[12]. At Hester Marsh, extensive diking and draining caused the area to subside and degrade to unvegetated mudflat. In 2018, ESNERR initiated a restoration project to reestablish healthy marsh ecosystems through soil addition, creating a high elevation marsh plain that is only inundated by the highest tides.

To assess relationships between marsh plant health and soil composition, soil property analyses including elemental analysis with a portable Hitachi XMET 8000 XRF (pXRF), were conducted in 2023 along ten permanent transects also monitored for vegetation. These compositional data serve as a baseline for elemental concentrations in soils prior to the 2025 battery fire (Table 1). Following the 16 January 2025 fire at the Moss Landing battery storage facility, three of the original transects were resampled at high spatial and temporal resolution between 21 January and 23 February 2025 (Tables S1 and S2).

During the 2023 survey, surface and subsurface (~5–10 mm depth) samples were collected to compare elemental concentrations above and below the shallow redox boundary characteristic of these tidal marsh soils.

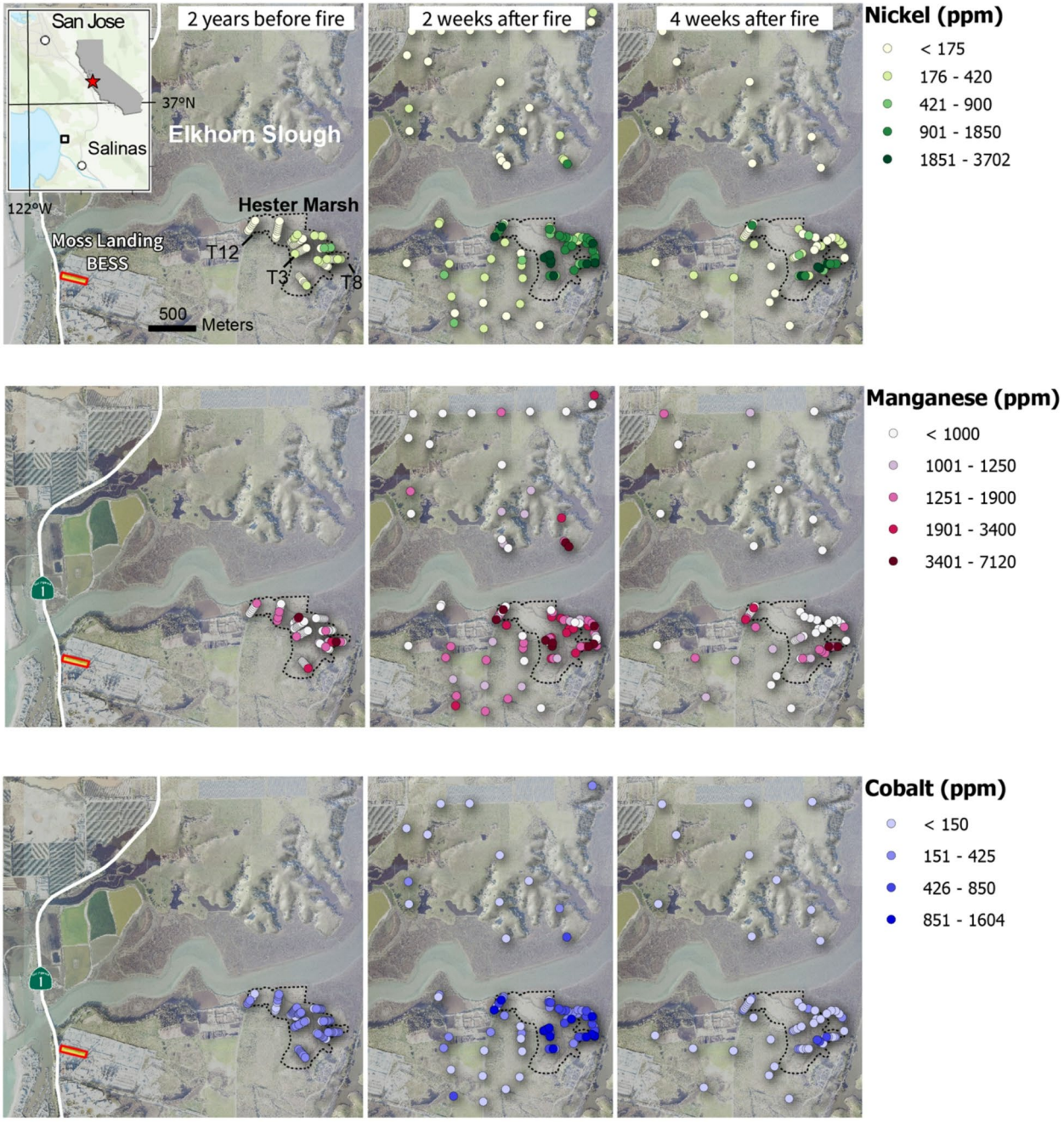

Fig. 2. Spatial distribution of nickel (Ni), cobalt (Co), and manganese (Mn) concentrations (ppm) in soils across three survey periods. The Hester Marsh restoration area is outlined with a dashed line and includes the locations of transects T12, T3, and T8. Peak concentrations were detected within this zone, approximately 1–3 km downwind of the Moss Landing battery facility. Color scales are consistent across all time points for each element to allow temporal comparison. Point classification for each element was done using the "Natural Breaks" (Jenks) method. The map was generated using ArcGIS Pro v3.4.2 (https://pro.arcgis.com/en/pro-app/latest/get-started/download-arcgis-pro.htm).

Additional measurements were taken both outside the transects and beyond the boundaries of Hester Marsh during two post-fire survey periods: post-fire#1 (21 January–12 February 2025) and post-fire#2 (18 February–27 March 2025) (see Supplementary Sect. 1). These post-fire surveys encompassed a broader area, including nearby grasslands within the surrounding watershed (Fig. 2). This approach incidentally enabled differentiation of recent fire-related metal deposition from background levels and allowed detection of a transient, spatially patchy signal. All FpXRF measurements across all surveys have been conducted on bare, relatively dry soils to minimize moisture-related biases.

			Surface												Subsurface†											
			Ni (ppm)				Mn (ppm)				Co (ppm)				Ni (ppm)				Mn (ppm)				Co (ppm)			
Survey period	Sites (*n*)	Area (km²)	min	max	median	MAD	min	max	median	MAD	min	max	median	MAD	min	max	median	MAD	min	max	median	MAD	min	max	median	MAD
Pre-fire (2023)	97	0.4	52	246	109	47	228	2193	713	315	72	298	183	59	52	232	116	43	324	2378	834	303	59	214	107	43
Post-fire#1 2025*	135	5.6	52	3702	441	517	386	7119	1488	783	40	1604	309	296	50	303	93	44	264	2119	926	435	40	218	91	49
Post-fire#2 2025^	64	5.6	52	339	100	49	45	3207	871	551	8	833	107	68	1	329	100	49	45	3207	871	551	8	265	97	56

Table . Summary statistics including minimum and maximum values, median, and median absolute deviation (MAD) of nickel (Ni), manganese (Mn), and Cobalt (Co) concentrations (ppm) in surface and subsurface soils measured by field-portable XRF (FpXRF) across three survey periods. Values represent minimum, maximum, and mean concentrations for each metal. †Subsurface measurements are from a few mm below the surface; *Post-fire#1 survey conducted Jan 21–Feb 12; ^Post-fire#2: Feb 18–Mar 27 (surface samples were measured in triplicate during Post-fire#2).

Soil samples collected in the field were analyzed using the pXRF in the lab (LpXRF) and with inductively coupled plasma mass spectrometry (ICP-MS) (Table S3).

Detailed laboratory procedures, including sample preparation, organic carbon analysis, and instrument protocols, environmental data, as well as statistical methods used for data analysis (non-parametric pairwise tests and regression analysis) and interpretation are provided in Supplementary Sect. 2.

Rain and tide data were retrieved from the Moss Landing weather station operated by Moss Landing Marine Laboratories and wind data from the ESNERR meteorological station (Tables S4 and S5).

Results

Detection and mapping of the cathode metals

Fragments of ash and burned or charred material were found scattered across Hester Marsh soils (Fig. 1b, c) in the days to weeks after the fire, providing clear physical evidence of fallout from the battery fire. The comparison between the 2023 and the 2025 post-fire data revealed a marked increase in concentrations of three metals: nickel (Ni), manganese (Mn), and cobalt (Co).

Notably, surface Ni and Co co-varied on log–log axes, with post-fire Ni: Co ratios averaging 2:1, consistent with NMC532 cathode chemistry. This fingerprint supports attribution of the (Ni, Mn, Co) metal spike to battery fire fallout.

Further analysis of selected samples using scanning electron microscopy (SEM) and energy-dispersive X-ray spectrometry (EDS) indicated that the elevated concentrations of Ni, Mn, and Co were linked to the presence of micron-sized metallic particles like those used as cathode materials in Nickel Manganese Cobalt (NMC) batteries. At finer scales, cathode-derived NMC microparticles were identified and elementally mapped in surface soil samples using SEM/EDS (Fig. 1d, e, f), consistent with the fracture and ejection of individual grains from NMC cathodes, a behavior previously observed in laboratory combustion tests[6]. These findings confirm the presence of fire-related battery material on the soil surface of nearby wetlands.

Geochemical evidence from FpXRF further supports the extent and magnitude of contamination. Although Ni, Mn, and Co displayed high spatial variability during the post-fire#1 survey, concentrations increased significantly relative to pre-fire values, with maximum Ni rising by an order of magnitude and Co by a factor of five (Table 1).

Overall, by the time the post-fire#2 survey was conducted, about 1 month after the battery fire, the median concentrations had decreased. The post-fire#1 subsurface data were statistically indistinguishable from the surface and subsurface 2023 pre-fire data. In contrast, surface concentrations of (Ni, Mn, Co) measured during the post-fire#1 survey were significantly elevated compared to pre-fire levels ($p < 0.001$, Mann–Whitney U test; Table S6), clearly indicating that the deposition associated with the fire was initially confined to the top layer of soil.

Figure 2 show that the post-fire#1 increase in metal concentrations (Ni, Mn, Co) in surface measurements was not uniform but clustered in distinct hotspots within Hester Marsh. Hester Marsh was also the area where the post-fire#2 survey recorded the most substantial decrease in metal concentrations. However, a few locations continued to show elevated levels, which explains why the maximum values of Ni and Co in the post-fire#2 survey remained high (Table 1). In contrast to the surface measurements, subsurface data showed no significant changes in either mean or maximum concentrations between the pre- and post-fire surveys. This further confirms that the sharp post-fire increase in cathode metal concentrations was confined to the topmost layer of the soil.

Although the FpXRF measurement along three permanent transects included the concentrations of all three cathode elements: Ni, Mn, and Co, we focused primarily on Ni as a tracer of battery fire fallout, as Ni is dominated by a single oxidation state (Ni^{2+}) across a broad range of redox and pH conditions. This makes it less sensitive to post-depositional remobilization compared to Mn and Co, both of which exhibit variable redox behavior in estuarine settings[13].

Mn is strongly influenced by fluctuations in redox potential and organic matter, and its concentrations often vary independently of anthropogenic inputs[14]. Co also exhibited substantial redox sensitivity and, notably, a large proportion of Co measurements were non-detects, especially in pre-fire and subsurface samples (Table S7), due to concentrations below the portable XRF instrument's relatively high detection limit (Ni ≈ 50 ppm, Mn ≈ 45 ppm, Co ≈ 40 ppm). Box plots depicting the temporal trends of surface Ni concentrations at three permanent transects show that, following the fire, the median Ni concentration increased by two to threefold compared to pre-fire levels (Fig. 3). Over the month-long survey period, both the median and interquartile range of concentrations declined, with a substantial drop to near pre-fire values observed in early February coincident with rainfall in the area. Notably, Ni concentrations rose again at all transects during the surveys conducted in the second half of February.

On log–log axes (Fig. 4a), surface Ni and Co show clear bivariate associations. The distribution of $\log_{10}$(Ni/Co) (Fig. 4b) shows that post-fire values average near the 2:1 reference (0.301), while pre-fire values average < 0 indicating a substantial change in surface soil metal composition following the fire.

Comparative elemental analysis: field versus lab

To compare FpXRF results with laboratory measurements, we collected 51 samples (24 subsurface and 27 surface) from soils that had previously been analyzed in the field with FpXRF after the battery fire. Aliquots of these samples were analyzed for moisture content, organic carbon content, and elemental composition using LpXRF (5–6 g) and ICP-MS (~ 0.25 g). The water content of the samples ranged from approximately 7 to 43% by weight, while organic carbon concentrations varied between 0.1% and 2.4% by weight.

Because regressions of XRF against the ICPMS reference had non-zero intercepts and modest R^2, we quantified method bias as the geometric mean of the per-sample ratios (i.e., FpXRF/ICPMS, LpXRF/ICPMS, and for completeness FpXRF/LpXRF, see Table S8). In subsurface samples, both XRF methods overestimated Ni

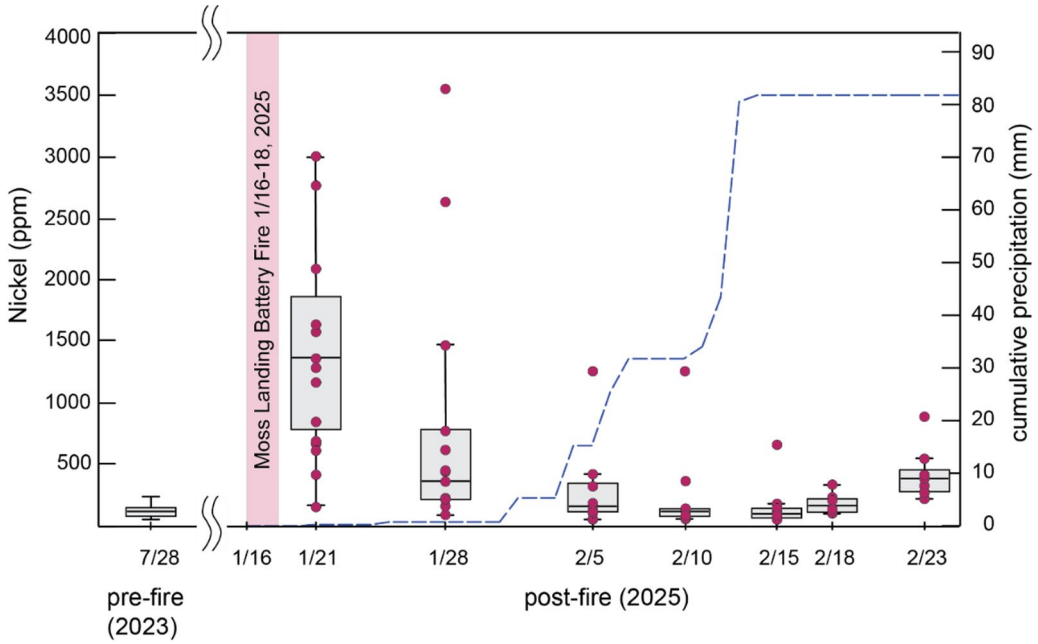

Fig. 3. Temporal variability in surface nickel (Ni) concentrations (ppm) along three permanent transects measured before the battery fire in 2023, and between January and February 2025 using field-portable X-ray fluorescence (FpXRF). Box plots represent the distribution of Ni concentrations at the benchmarks along each transect measured during each sampling date. The datapoints are represented with red circles (the pre-fire survey data were not included because they were indistinguishable and overlapping given their low values). The dashed line shows cumulative precipitation data recorded at the Moss Landing Marine Laboratories weather station (Latitude: 36.80040° N, Longitude: 121.78842° W). A transient spike in Ni concentrations occurred immediately after the 16 January 2025 battery fire, followed by a rapid decline, likely associated with rainfall and tidal flushing in early February. A smaller secondary increase was observed in late February, coinciding with the 18 February 2025 reignition event.

relative to ICPMS by roughly threefold (FpXRF/ICPMS = 3.09, 95% CI 2.74–3.48; LpXRF/ICPMS = 2.81, 95% CI 2.61–3.02), while the two types of XRF measurements were in reasonable agreement (FpXRF/LpXRF = 1.10, 95% CI 0.97–1.25). In surface samples, both FpXRF and LpXRF exhibited a larger positive bias (FpXRF/ICP-MS = 5.40, 95% CI 4.18–6.99; LpXRF/ICP-MS = 2.33, 95% CI 1.93–2.81). As we describe below, the stronger disagreement between FpXRF and laboratory measurements at the surface is best explained by dilution of a thin, metal-rich veneer during laboratory homogenization (which mixes surface material with underlying soil), whereas in-situ FpXRF interrogates the veneer more directly.

As observed with FpXRF data, LpXRF measurements of subsurface samples showed no significant linear association between Co and Ni. In contrast, surface samples showed coherent Ni–Co covariation across methods; Ni: Co ratios were near 2:1, consistent with Fig. 4b and the Ni-to-Co ratio observed in the post-fire#1 FpXRF survey data (Table S9).

Depth distribution of cathode metals

The NMC microparticles primarily occurred as aggregates of varying shape and size, often ~ 100 µm or larger (Fig. 1d, f). This suggests a minimum thickness for the deposition layer of approximately 100 µm, comparable to the critical detection depths for Ni, Mn, and Co in XRF analysis, defined as the depth beyond which less than 1% of the original fluorescent signal reaches the detector.

A rough estimate of the thickness of this contaminated layer can be derived by comparing FpXRF measurements with LpXRF results from sliced surface samples for which lab-based measurements using both LpXRF and ICP-MS yielded lower concentrations of Ni, Mn, and Co compared to those obtained via FpXRF.

Our hypothesis was that FpXRF and LpXRF should approximately yield similar concentrations (i.e., FpXRF/LpXRF ≈ 1) only when the thickness of the lab-analyzed sample approaches the depth of the metal-enriched layer. If the sample is thicker, it will include subsoil not affected by the fire, diluting the signal and resulting in FpXRF/LpXRF > 1.

A regression analysis of sample thickness versus the FpXRF/LpXRF ratio revealed a moderate positive linear association ($R^2 = 0.30$, $p = 0.0129$) that should be interpreted with caution. However, the ratio approaches one for samples between ~ 2 and 5 mm thick, which we interpret as the approximate depth to which fire-related cathode metals were initially incorporated into the soil (Figure S3).

This finding is consistent with our surface method comparison against the ICPMS reference: as the effective field sampling depth increases, the measured signal is increasingly diluted by pre-fire baseline material, leading

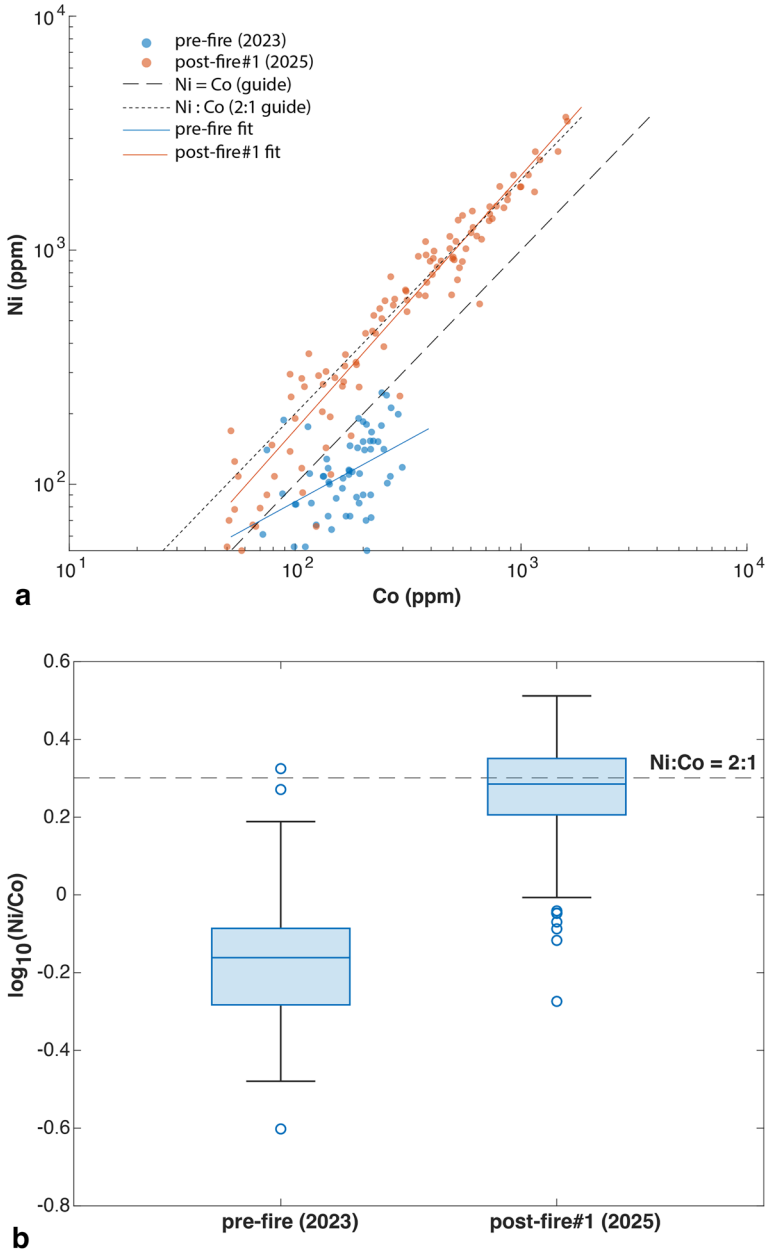

Fig. 4. (**a**) Log–log scatter of Co versus Ni (ppm; FpXRF) for pre-fire (2023, blue) and post-fire#1 (Jan–Feb 2025, orange). Guidelines show Ni = Co (1:1) and Ni: Co = 2:1. Robust log–log fits: pre b = 0.45 (95% CI 0.25–0.65); post b = 0.85 (0.80–0.89). (**b**) Distributions of $\log_{10}$(Ni/Co) for the same samples; dashed line at 0.301 marks Ni: Co = 2:1. Post-fire medians lie near 2:1, whereas pre-fire values are < 0.

to underestimation of battery fire-related surface contamination (see Supplementary Sect. 2 for a detailed discussion of pXRF detection depth and matrix effects).

Discussion

Rapid detection of cathode metals with FpXRF

The sharp increase in (Ni, Mn, Co) metal concentrations detected in the surface soils of Hester Marsh between late January and early February 2025 is clearly attributable to the deposition of particulate matter from the smoke plume generated by the nearby battery storage facility fire at Moss Landing just days earlier. This interpretation is supported by multiple lines of evidence, including visible ash residues and soot, the presence of cathode-derived microparticles in surface soils, and distinctive geochemical patterns.

The key to early detection of cathode metal fallout immediately after the Moss Landing battery fire was the use of FpXRF. While field measurements were not as accurate as lab measurements, they played a pivotal role in rapidly observing that maximum concentrations of the three metals increased by an order of magnitude after the fire, monitoring how quickly they decreased, and assessing how patchy the battery metal fallout was across

the landscape. This key information could have been completely missed if we had relied only on a handful of samples taken in space and time. Metal co-variation patterns were consistent across methods (FpXRF, LpXRF, ICP-MS), while absolute levels differed.

While the use of FpXRF offers substantial advantages in responding quickly to environmental emergencies like battery fires, it also comes with limitations. These are especially pronounced in wetland soils, where moisture content, organic matter, and textural variability can significantly influence the accuracy of XRF readings. Light elements such as Ni, Mn, and Co are particularly susceptible to overestimation when measured with XRF, compared to more precise ICP-based methods[15–18]. Our comparison of field and laboratory measurements confirms this pattern: both FpXRF and LpXRF overestimated Ni concentrations by more threefold relative to ICP-MS in the subsurface where samples do not include the fallout deposit.

Nevertheless, the methods showed an acceptable level of reproducibility, supporting the reliability of XRF for rapid environmental assessment. Importantly, although absolute concentrations may be overestimated, the change in surface concentrations before and after the fire was evaluated using the same FpXRF method, allowing for robust spatial comparison and comparison of relative differences over time.

A fingerprint for the cathode material

On log–log axes, Ni scales with Co in surface soils (Fig. 4a). Using ordinary least squares (OLS), the pre-fire fit yields b = 0.4750b and a = 0.9913 ($R^2 = 0.175$), indicating a heterogeneous pre-fire ambient signal. The post-fire (survey 1) yields b = 1.1023 and a = 0.0061 ($R^2 = 0.912$); the point cloud and fitted line lie close to the Ni = 2·Co guideline across the observed range, motivating a ratio view.

Figure 4b shows that the distribution of $\log_{10}$(Ni/Co) shifts from pre-fire values < 0 (Ni: Co < 1) to post-fire values near the 2:1 reference ($\log_{10}2 = 0.301$). This composition is consistent with the NMC532 cathode chemistry used in lithium-ion batteries[19].

Subsurface samples remained near pre-fire levels and did not exhibit the post-fire ratio shift, indicating enrichment confined to a surface veneer. Notably, maximum surface concentrations of all three metals increased by several fold relative to pre-fire levels (Table 1). Most post-fire#1 surface samples analyzed with ICP-MS had Ni concentrations above 50 ppm, values that exceed thresholds associated with toxicity risks to plants and aquatic organisms[20].

The observed changes in surface concentrations of Ni, Mn, and Co across Hester Marsh and surrounding areas over time indicate the potential for rapid remobilization of these transition metals into estuarine soils and downstream waters (Fig. 2). FpXRF transect data from February–March 2025 show that surface Ni concentrations dropped to near baseline within weeks of the fire, following early February rain and tidal inundation (Fig. 3).

While variability in Ni concentrations declined over time, indicating redistribution of the cathode metals, at the higher elevation transect T12 (~ 1 km from the fire), higher Ni levels persisted for about 10 days before declining, while the lower elevation transects T3 and T8 showed an earlier decrease, likely due to January tidal flooding that immersed only the areas with the lowest relief.

The transect data and a simple comparison between columns 2 and 3 in Fig. 2 illustrate that had FpXRF sampling been delayed by even a few days, most of the early evidence for surface deposition in Elkhorn Slough would likely have been lost. Timely field deployment was essential for capturing the initial contamination signal before environmental processes such as rainfall and tidal flushing remobilized the metals.

Our results emphasize the high degree of spatial variability in the distribution of battery-associated metals on the soil surface. The highest concentrations observed after the fire were within the unvegetated portions at Hester Marsh (Fig. 2). Concentrations were also highly variable at finer spatial scales, between samples collected 10–20 m apart along the transects.

Boxplots of Ni concentrations over time along three transects (Fig. 3) show that the interquartile range, a measure of variability excluding outliers, increases with the median concentration. This relationship suggests that spatial heterogeneity is greatest where concentrations are highest, a pattern we interpret as evidence of the clumped distribution of cathode metal-bearing particles or ash. At the microscale, this clumping is represented by aggregates of NMC microparticles (Fig. 1d–f); at the macroscale, it is reflected in the scattering of ash and burned material fragments observed throughout the study area, up to approximately 3 km from the battery storage facility (Fig. 1b, c). Larger clumps result in higher localized concentrations and contribute to measurement variability, reinforcing the importance of repeated sampling at multiple spatial scales. This multi-scale capability is one of the key advantages of FpXRF over conventional discrete sampling and ensuing analysis via ICP-MS.

The relationship between the FpXRF/LpXRF concentration ratio and sample thickness used to estimate the critical depth of Ni enrichment following the battery fire shows that the ratio approaches 1.0 when sample thicknesses range between ~ 2 and 5 mm, suggesting that most of the deposited Ni was confined to the uppermost few millimeters of soil. Thicker samples diluted this surface signal, consistent with a sharp depositional pulse and limited vertical mixing. This interpretation aligns with both SEM imaging of NMC microparticle aggregates and the shallow critical escape depth of Ni in soil matrices.

Tracking the environmental footprint of cathode material

The cathode material detected in Elkhorn Slough soils following the battery fire was, at least initially, airborne. As a first approximation, the spatial distribution of cathode metals observed in surface soils during the post-fire#1 survey reflects the deposition pattern of battery-derived particulates that settled from the smoke plume. However, this interpretation likely oversimplifies the dynamics. Prior studies show that ground-level deposition often diverges from the plume's direction due to complex atmospheric behavior, as additional factors might be influencing spatial variability including plume height, particle size and shape, and sorptive properties of the soil surface[21,22].

Our reconstruction of the (Ni, Mn, Co) metal distribution from the post-fire#1 survey reveals that surface concentrations of contaminants do not increase with proximity to the battery fire site. Instead, concentrations peak in the Hester Marsh wetland, located approximately 1–3 km east of the facility (Fig. 2). This offset may be explained by westerly surface winds on the day of the fire, which prevailed for approximately 40% of the time, likely directing the smoke plume eastward over Hester Marsh (Fig. 1a). In addition to wind direction, local soil characteristics may have played a role in the retention of the metal particles following deposition. Hester Marsh soils are predominantly fine-grained and clay-rich, with high sorptive capacity, and higher potential for retention of transition metals that can increase their persistence in surface layers[23,24].

Regardless of the factors that controlled the initial distribution and retention of material deposited from the battery fire, the spike in transition metal concentrations at the surface of the wetland was short-lived. By the time the post-fire#2 survey was conducted, most of the cathode metals accumulated on the surface soils had been remobilized, except for a few persistent hotspots in some of the depressional salt pans within Hester Marsh (Fig. 2).

Natural processes such as rainfall and tidal inundation likely played a major role in the resuspension and remobilization of the contaminants. Precipitation was relatively intense during the first 2 weeks of February 2025 (Fig. 3), and the lower portions of Hester Marsh experienced repeated inundation during high-tide events, facilitating the physical transport and dispersal of deposited cathode metals. Percolation through the soils appears to have been limited since the post-fire#2 and post-fire#1 subsurface concentrations were statistically indistinguishable.

The drop in surface concentration of cathode metals resulting from the battery fire strongly suggests that the metals have been washed into downstream portions of the estuarine ecosystem. Their transport and fate throughout the estuary and potentially into adjacent open coastal ecosystems remain unknown. They may have settled in tidal channels, become buried in sediments, or undergone chemical transformations driven by redox cycling[25].

These processes could affect both metal mobility and, over time, pose a threat to higher trophic levels through bioaccumulation. Ni, Mn, and Co are all known to be toxic to humans as well as to aquatic and terrestrial organisms[20], and Mn toxicity is a major constraint limiting plant growth and production[16]. Co can have lethal or sublethal effects on reproduction in fish and crustaceans and has some bioaccumulation potential through adsorption to plant roots[26]. These risks are particularly acute at Hester Marsh, where an $18 M investment to restore tidal wetlands through soil augmentation raised marsh platforms to elevations intended to sustain native plant growth and survival under future flooding[27].

Mass budget for cathode metal deposition at Hester Marsh

The initial mass of Ni, Mn, and Co originating from the burned batteries that settled on Hester Marsh can be estimated based on the difference between metal concentrations measured at the surface during the pre-fire and the post-fire#1 surveys (see Table S10 for full calculations). To calculate the mass budget, the Hester Marsh area (1200,000 m^2) was overlain with a 200 × 200 m grid composed of 30 cells, each covering a 40,000 m^2 area. For 10 of the 30 cells that contained both pre-fire and post-fire#1 FpXRF measurements, we computed the paired mean difference (post-fire#1—pre-fire) and the standard errors. The concentrations of the three metals were then converted to mass assuming a surface contamination depth of approximately 0.1 mm (which approximates the critical detection depth for these metals) and a dry density of 1500 kg/m^3 for consolidated clay.

We estimate that the minimum deposited mass of cathode metals within the upper 100 μm is ~ 17 kg ± 4 kg per 200 × 200 m cell. However, as discussed earlier, the actual thickness of the soil layer containing the deposited metals is likely greater than the effective depth, and can be ~ 5 mm thick, which corresponds to a mass of cathode metals of ~ 855 kg ± 199 kg per cell. Extrapolation to the entire Hester Marsh area yields an estimated total mass of cathode metals of ~ 25 metric tons (25676 kg ± 5981 kg).

This estimate should be interpreted with caution. First, FpXRF measurements overestimate Ni concentrations by a factor of ~ 3, and the metal concentrations are expected to decline with depth due to dilution and limited vertical mixing. However, the values are also conservative, as they only include deposition on bare soil and exclude potential accumulation on vegetation, which may represent a larger surface area in marsh and upland settings than the exposed soil itself.

To put these figures in perspective, a 1 MW industrial lithium-ion battery manufactured by LG weighs 1.6 metric tons, with cathode materials accounting for approximately 35% of the total mass. This equates to roughly 1900 metric tons for the entire 1200 MWh storage capacity of the Moss Landing facility. If, as reported by Monterey County officials[10], approximately 75% of the batteries were destroyed in the fire, then an estimated ~ 1400 metric tons of cathode material could have been involved in the event and potentially entrained into the smoke plume. Therefore, our estimates of the total mass of (Ni, Mn, Co) metals deposited on the soils of the Hester Marsh extrapolated to a 5 mm cathode metal deposit accounts only for < ~ 2% of the total battery material that may have been released during the Moss Landing battery fire.

Conclusions and implications for future battery fire response

To our knowledge, this study represents the first field-based documentation of battery-associated metal fallout following a large-scale lithium-ion battery fire and offers a framework for assessing future events of this kind. Use of field instrumentation enabled immediate collection of hundreds of measurements, critical given the spatial patchiness of battery metal aggregates in an extensive fallout layer in the vicinity of the fire and given the rapidity with which the metals were transported downstream by tides and rain. As battery energy storage systems continue to expand in scale and density, the risk of both localized and widespread contamination will increase even as safety protocols improve.

This incident also calls attention to the limitations of standard environmental sampling protocols. Conventional soil sampling depths, such as the commonly used top ~ 6 cm of soil[28], may fail to detect thin, spatially heterogeneous deposition layers. The patchy nature of ash deposition observed in this study suggests that sampling strategies must be adaptive and designed to capture contamination at multiple spatial scales and depths. This is especially critical in the first few days following an event, since, over time, rainfall, tides, and wind can rapidly redistribute surface-bound contaminants.

Environmental response frameworks must also consider the potential offset between fire origin and deposition zones. In this case, the most significant contamination occurred not adjacent to the site of the fire, but several kilometers downwind. This spatial offset highlights the need for evacuation protocols and monitoring networks that integrate plume dispersion models, meteorological data, air quality monitoring and ground-based measurements of deposition.

Finally, findings from controlled laboratory battery burns provide additional context for interpreting field observations. Previous experiments have demonstrated that thermal decomposition of cathode materials can release substantial quantities of (Ni, Mn, Co) metals and other toxicants[6]. These studies confirm that NMC-based batteries, when subjected to fire conditions, can emit airborne particles capable of traveling significant distances before settling onto the landscape. Field studies such as this one are essential to understanding how such deposition events unfold under real-world conditions.

Together, these results emphasize the need for proactive planning, site-specific risk assessment, and rapid, multi-scale environmental monitoring in the aftermath of battery fires. As battery technologies evolve, so too must the frameworks we use to track and mitigate their potential environmental impacts.

Data availability

All data used to generate the figures are available through Figshare at https://figshare.com/s/32fb2899e519353f923b **.**.

Received: 14 August 2025; Accepted: 27 October 2025
Published online: 26 November 2025

References

1. Koohi-Fayegh, S. & Rosen, M. A. A review of energy storage types, applications and recent developments. *J. Energy Storage* **27**, 101047. https://doi.org/10.1016/j.est.2019.101047 (2020).
2. Gutsch, M. & Leker, J. Global warming potential of lithium-ion battery energy storage systems: A review. *J. Energy Storage* **52**, 105030. https://doi.org/10.1016/j.est.2022.105030 (2022).
3. Gür, T. M. Giga-ton and tera-watt scale challenges at the energy-climate crossroads: A global perspective. *Energy* **290**, 129971. https://doi.org/10.1016/j.energy.2023.129971 (2024).
4. Armand, M. et al. Lithium-ion batteries—current state of the Art and anticipated developments. *J. Power Sources* **479**, 228708. https://doi.org/10.1016/j.jpowsour.2020.228708 (2020).
5. Xie, J., Li, J., Wang, J., Jiang, J. & Shu, C. M. Fire risk assessment in lithium-ion battery warehouse based on the bayesian network. *Process. Saf. Environ. Prot.* **176**, 101–114. https://doi.org/10.1016/j.psep.2023.06.005 (2023).
6. Barone, T. L. et al. Lithium-ion battery explosion aerosols: Morphology and elemental composition. *Aerosol Sci. Technol.* **55**, 1183–1201. https://doi.org/10.1080/02786826.2021.1938966 (2021).
7. Mrozik, W., Rajaeifar, M. A., Heidrich, O. & Christensen, P. Environmental impacts, pollution sources and pathways of spent lithium-ion batteries. *Energy Environ. Sci.* **14**, 6099–6121. https://doi.org/10.1039/D1EE00691F (2021).
8. Lopez, R. D. *Ramsar Wetlands of the North American West Coast and Central Pacific: An Atlas* (CRC, 2024). https://doi.org/10.1201/9781003046394
9. Vistra Corp. Vistra completes expansion of battery energy storage system at its flagship California facility. https://investor.vistracorp.com/2021-08-19-Vistra-Completes-Expansion-of-Battery-Energy-Storage-System-at-its-Flagship-California-Facility (Accessed 29 September 2025).
10. San Francisco Chronicle. Fire at California battery plant brings safety assurances, quest for answers. San Francisco Chronicle (18. Jan (2025). https://www.sfchronicle.com/california/article/moss-landing-fire-20042587.php (Accessed 29 September 2025).
11. County of Monterey. Moss Landing Power Plant Fire. https://www.readymontereycounty.org/emergency/2025-moss-landing-vistra-power-plant-fire (Accessed 29 September 2025).
12. Van Dyke, E. & Wasson, K. Historical ecology of a central California estuary: 150 years of habitat change. *Estuaries* **28**, 173–189. https://doi.org/10.1007/BF02732853 (2005).
13. Yang, Z., Guo, W., Fan, Y., Lin, C. & He, M. High-resolution profiles of iron, manganese, cobalt, cadmium, copper and zinc in the pore water of estuarine sediment. *Int. J. Environ. Sci. Technol.* **10**, 275–282. https://doi.org/10.1007/s13762-012-0110-2 (2013).
14. Bartlett, R. J. Manganese redox reactions and organic interactions in soils. In Manganese in Soils and Plants (eds (eds Graham, R. D., Hannam, R. J. & Uren, N. C.) 59–73 (Springer, Dordrecht, 1988). https://doi.org/10.1007/978-94-009-2817-6_5
15. Sikora, A. L., Maguire, L. W., Nairn, R. W. & Knox, R. C. A comparison of XRFS and ICP-OES methods for soil trace metal analyses in a mining-impacted agricultural watershed. *Environ. Monit. Assess.* **193**, 92. https://doi.org/10.1007/s10661-021-09275-9 (2021).
16. Li, W. et al. Comparative study on the determination of heavy metals in soil by XRF and ICP-MS. *J. Phys. : Conf. Ser.* **2009** (012075). https://doi.org/10.1088/1742-6596/2009/1/012075 (2021).
17. Ge, L., Lai, W. & Lin, Y. Influence of and correction for moisture in rocks, soils and sediments on in situ XRF analysis. *X-Ray Spectrom.* **34**, 28–34. https://doi.org/10.1002/xrs.782 (2005).
18. Wilson, P., Cooke, M., Cawley, J., Giles, L. & West, M. Comparison of the determination of copper, nickel and zinc in contaminated soils by X-ray fluorescence spectrometry and inductively coupled plasma spectrometry. *X-Ray Spectrom.* **24**, 103–108. https://doi.org/10.1002/xrs.1300240305 (1995).
19. ECHA. Lithium nickel cobalt manganese oxide. European Chemicals Agency. https://echa.europa.eu/ (Accessed 29 September 2025).
20. Eisler, R. Nickel hazards to fish, wildlife, and invertebrates: A synoptic review. US Geological Survey, Patuxent Wildlife Research Center. https://restservice.epri.com/publicdownload/000000003002030360/0/Product (Accessed 29 September 2025).
21. Lejon, C. et al. Lagrangian plume rise and dispersion modelling of the large-scale lithium-ion battery fire in Morris, USA, Air Qual. Atmos. Health 17, 2077–2089 (2024). https://doi.org/10.1007/s11869-023-01443-9 (2021).
22. Goodrick, S. L., Achtemeier, G. L., Larkin, N. K., Liu, Y. Q. & Strand, T. M. Modelling smoke transport from wildland fires: A review. *Int. J. Wildland Fire* **22**, 83–94. https://doi.org/10.1071/WF11116 (2013).

23. Shand, C. A. & Wendler, R. Portable X-ray fluorescence analysis of mineral and organic soils and the influence of organic matter. *J. Geochem. Explor.* **143**, 31–42. https://doi.org/10.1016/j.gexplo.2014.03.005 (2014).
24. Kravchenko, E. et al. Ecological and health risk assessments of heavy metal contamination in soils surrounding a coal power plant. *J. Hazard. Mater.* **484**, 136751. https://doi.org/10.1016/j.jhazmat.2024.136751 (2025).
25. Barrio-Parra, F. et al. Environmental risk assessment of Cobalt and manganese from industrial sources in an estuarine system. *Environ. Geochem. Health* **40**, 737–748. https://doi.org/10.1007/s10653-017-0020-9 (2018).
26. ATSDR. Toxicological Profile for Cobalt. https://www.atsdr.cdc.gov/toxprofiles/tp33.pdf (Accessed 29 September 2025).
27. Haskins, J. et al. UAV to inform restoration: A case study from a California tidal marsh. *Front. Environ. Sci.* **9**, 642906. https://doi.org/10.3389/fenvs.2021.642906 (2021).
28. US EPA. Method 6200: Field portable X-ray fluorescence spectrometry for the determination of elemental concentrations in soil and sediment. https://www.epa.gov/sites/default/files/2015-06/documents/6200.pdf (Accessed 29 September 2025).

Acknowledgements

We are deeply grateful to Julie Packard, Nancy Burnett, and Louise Stephens for their generous support and long-standing commitment to environmental research and conservation. We also thank the Monterey Bay Aquarium and the Simpkin Family for their crucial contributions, which made this work possible. Their support has been instrumental in enabling rapid response science and advancing our understanding of environmental risks in estuarine ecosystems. A grant from NOAA's Office for Coastal Management in support of the Elkhorn Slough National Estuarine Research Reserve (ESNERR) provided funding for KW and CE. The fortuitous pre-fire baseline was made possible due to ESNERR's heavy investment in restoration monitoring at Hester Marsh with grants from the California Department of Fish and Wildlife Greenhouse Gas Reduction Program, Ocean Protection Council and USFW National Coastal Wetland Program. The majority of data for this study come from ESNERR, a partnership between California Department of Fish and Wildlife and NOAA, and we are grateful for ESNERR's support of the study. We acknowledge MLML/Marine Pollutions Study Lab staff members Autumn Bonnema, Adam Newman, and April Sjoboen Guimaraes for ICP-MS sample digestions and analysis. Two anonymous reviewers provided thoughtful suggestions that improved the presentation of data and the clarity of writing.

Author contributions

I.W.A conceived the study, led the writing and contributed to all aspects of this work; CE performed field work, data collection and geospatial interpretations; SC performed lab analyses; MF contributed to study design, site access and data collection; MG contributed to data interpretation; WH performed lab analysis and data interpretation; AK contributed to data interpretation; KW contributed to study design, site access and data interpretation. All authors contributed to manuscript revisions and approved the final version.

Declarations

Competing interests

The authors declare no competing interests.

Additional information

Supplementary Information The online version contains supplementary material available at https://doi.org/10.1038/s41598-025-25972-8.

Correspondence and requests for materials should be addressed to I.W.A.